iScience

CellPress
OPEN ACCESS

Article

Polysphaeroides filiformis, a proterozoic cyanobacterial microfossil and implications for cyanobacteria evolution

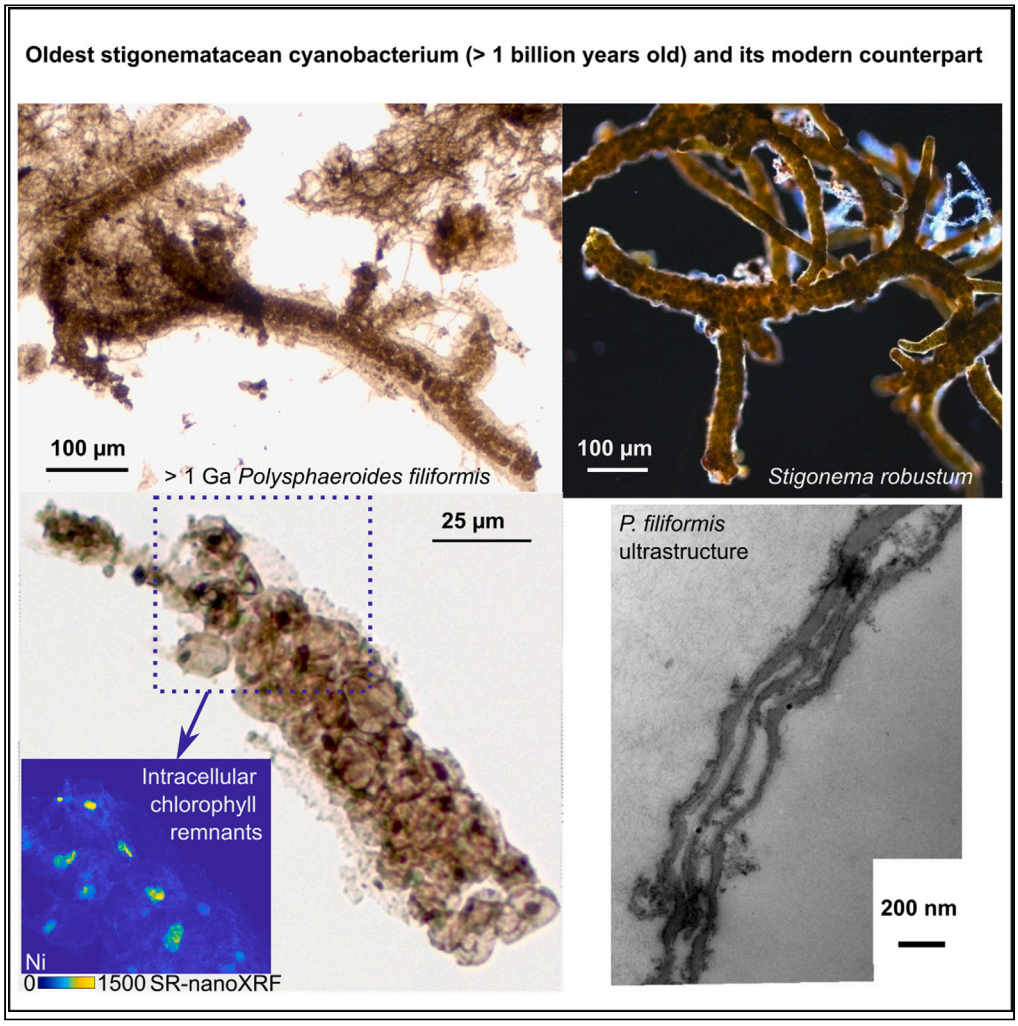

Catherine F. Demoulin, Marie Catherine Sforna, Yannick J. Lara, ..., Alexandre Fadel, Philippe Compère, Emmanuelle J. Javaux

ej.javaux@uliege.be

Highlights

Multiproxy approach elucidates >1 billion years microfossil identity

Oldest stigonematacean cyanobacterium is 600 Ma older than previously reported

Latest evolving true-branching already occurred during the late Mesoproterozoic

New calibration point for heterocytous nitrogen-fixing true-branching cyanobacteria

Demoulin et al., iScience 27, 108865
February 16, 2024
https://doi.org/10.1016/j.isci.2024.108865

iScience

CellPress
OPEN ACCESS

Article

Polysphaeroides filiformis, a proterozoic cyanobacterial microfossil and implications for cyanobacteria evolution

Catherine F. Demoulin,[1] Marie Catherine Sforna,[1,2] Yannick J. Lara,[1] Yohan Cornet,[1] Andrea Somogyi,[3] Kadda Medjoubi,[3] Daniel Grolimund,[4] Dario Ferreira Sanchez,[4] Remi Tucoulou Tachoueres,[5] Ahmed Addad,[6] Alexandre Fadel,[6] Philippe Compère,[7] and Emmanuelle J. Javaux[1,8,*]

SUMMARY

Deciphering the fossil record of cyanobacteria is crucial to understand their role in the chemical and biological evolution of the early Earth. They profoundly modified the redox conditions of early ecosystems more than 2.4 Ga ago, the age of the Great Oxidation Event (GOE), and provided the ancestor of the chloroplast by endosymbiosis, leading the diversification of photosynthetic eukaryotes. Here, we analyze the morphology, ultrastructure, chemical composition, and metals distribution of *Polysphaeroides filiformis* from the 1040–1006 Ma Mbuji-Mayi Supergroup (DR Congo). We evidence trilaminar and bilayered ultrastructures for the sheath and the cell wall, respectively, and the preservation of Ni-tetrapyrrole moieties derived from chlorophyll in intracellular inclusions. This approach allows an unambiguous interpretation of *P. filiformis* as a branched and multiseriate photosynthetic cyanobacterium belonging to the family of Stigonemataceae. It also provides a possible minimum age for the emergence of multiseriate true branching nitrogen-fixing and probably heterocytous cyanobacteria.

INTRODUCTION

Unraveling the timing and pattern of evolution of early cyanobacteria is of prime importance to understand their impact on the evolution of early life and Earth. Cyanobacteria are the only prokaryotes able to perform oxygenic photosynthesis. This metabolism,[1] and perhaps crown group cyanobacteria,[2] may have appeared as early as the Archean and, with tectonic and magmatic events, led to the Great Oxidation Event (GOE) around 2.4 Ga[3,4] and to other possible earlier low-oxygenation events.[5] As a consequence of early redox fluctuations, new ecological niches developed at several spatial and time scales.[6] Cyanobacteria were the main primary producers in the Proterozoic and played an important role in the carbon cycle before the rise of eukaryotic algae.[7] Cyanobacteria are also directly involved in the diversification of photosynthetic eukaryotes as the ancestors of the chloroplast, the organelle where oxygenic photosynthesis takes place within eukaryotic photosynthetic organisms,[8] and indirectly in the origin or diversification of early aerobic eukaryotes close to cyanobacterial mats.[9]

The presence of cyanobacteria during the Precambrian is also evidenced by the characterization of molecular fossils of chlorophyll and carotenoid derivatives in 1.1 Ga and 1.73 Ga bitumens, respectively.[10,11] Although the cyanobacterial origin was confirmed by the N isotopic ratio of the 1.1 Ga geoporphyrins,[10] 1.73 Ga carotenoid derivatives could also originate from green sulfur bacteria.[11] Carbon isotopes compositions measured on silicified microfossils from 1.56 Ga and 0.85 Ga cherts were compared to carbon isotopes values resulting from carbon fixation by the RubisCO enzyme in oscillatorian cyanobacteria.[12] Finally, stromatolites and microbially induced sedimentary structures (MISS) were commonly attributed to cyanobacterial benthic macroscopic formations because of their importance in modern mats. However, this does not insure their presence in Precambrian mats, since other microorganisms, such as anoxygenic photosynthesizers or methanotrophs are also involved in the formation of these structures, and may coexist with archaea and protists, suggesting they are not biosignatures specific of cyanobacteria.[13–15]

The oldest recorded cyanobacterial microfossil is *Eoentophysalis belcherensis*, identified in stromatolites of the Belcher islands, Canada,[16,17] and dated between 2018.5 and 2015.4 Ma.[18] *E. belcherensis* displays a morphology and cell division mode that are similar to those

[1]Early Life Traces & Evolution-Astrobiology, UR Astrobiology, University of Liège, 4000 Liège, Belgium
[2]Centre de Biophysique Moléculaire, (UPR CNRS 4301), 45071 Orléans, France
[3]Synchrotron Soleil, 91190 Saint-Aubin – BP 48, France
[4]Paul Scherrer Institut, Swiss Light Source, 5232 Villigen PSI, Switzerland
[5]ESRF-The European Synchrotron, 38000 Grenoble, France
[6]Unité Matériaux et Transformations (UMR CNRS 8207), Université Lille 1 - Sciences et Technologies, 59650 Villeneuve d'Ascq, France
[7]Functional and Evolutive Morphology, UR FOCUS, and Center for Applied Research and Education in Microscopy (CAREM-ULiege), University of Liège, 4000 Liège, Belgium
[8]Lead contact
*Correspondence: ej.javaux@uliege.be
https://doi.org/10.1016/j.isci.2024.108865

of the modern cyanobacterial genus *Entophysalis*.[16] The combination of these morphological traits and division patterns, exclusively found among cyanobacteria, and their microscopic distribution indicative of phototropism within stromatolites, enabled their unambiguous interpretation (review in a study by Demoulin et al[19]). Likewise, *Polybessurus* and *Eohyella* were identified as cyanobacteria with certainty based on the same criteria. These criteria are following the taxonomy of modern cyanobacteria based on the occurrence of uni- or multicellularity, pattern of cell division, the presence of a sheath, of baeocytes and other specialized cells (akinetes and heterocytes), and of true or false branching of filaments. Akinetes are dormant cells enabling cyanobacteria to survive in harsh environmental conditions and their reproduction by germination when conditions improve.[20–23] Heterocytes are specialized cells used as anoxic compartments for nitrogen fixation.[24] These two types of specialized cells occur in cyanobacteria belonging to the order Nostocales.[25] The presence of true branching in cyanobacteria occurs in several members of the Hapalosiphonaceae, Stigonemataceae, Gleitleriaceae, and Rhizonemataceae families.[26,27] However, the lack of other specific signatures leads to uncertainties as some of these traits can be present in other bacterial or eukaryotic taxa. Several authors proposed a possible nostocalean, or sometimes more specifically stigonematacean, interpretation for some microfossils such as *Polysphaeroides filiformis*, *Chlorogloeaopsis*, *Archaeoellipsoides*, *Navifusa*, *Orculiphycus*, *Glenobotrydion*, *Polytrichoides*, *Uroniopsora*, *Filiconstrictosus*, and *Ramivaginalis*.[28–33] Moreover, Pang et al. (2018) interpreted some microfossils (*Anhuithrix magna*) as N-fixing heterocytous cyanobacteria, implying the presence of Nostocales between 1000 and 720 Ma.[34] However, although these interpretations may be rightly attributed in most cases, they were exclusively based on morphology and need more support with stronger evidence. Before this report, the oldest unambiguous observation of a Stigonematacean cyanobacterium would be *Rhystigonema obscurum*, a microfossil from the famous 411.5 ± 1.3 Ma–407 ± 2.6 Ma Rhynie Chert assemblage.[35]

In a previous review, Demoulin et al. (2019) proposed to distinguish unambiguous cyanobacterial microfossils from probable and possible cyanobacterial microfossils based on the degree of confidence of diagnostic criteria.[19] To date, *Polysphaeroides filiformis* was interpreted as a probable cyanobacterium because some of its morphological traits also occur in other organisms, such as green or red eukaryotic algae.[19,32,36,37] *P. filiformis* was first described by Hermann in 1976 as a microfossil consisting of vesicles arranged into a multiseriate filament surrounded by a common sheath.[28] The genus *Polysphaeroides* is now only represented by the sheathed species *P. filiformis* since Hofmann and Jackson[38] have moved all the other unsheathed species of *Polysphaeroides* into the genus *Chlorogloeaopsis*. *P. filiformis* has been identified in six formations during the Proterozoic (see Table S1). Its oldest occurrence is dated back to 1483 ± 100 Ma in the Ust'-il'ya Formation and in the 1457 ± 220 Ma Kotuikan Formation, both formations belong to the Billyakh Group, Siberia.[39–41] However, branching was reported for the first time only in a well-preserved specimen from the 1040–1006 Ma Mbuji-Mayi Supergroup, DRC.[42,43] In 2019, Demoulin et al.[19] proposed *Stigonema robustum*, a branching stigonematacean heterocytous cyanobacterium, as a remarkably similar possible modern analogue of *P. filiformis*.

To thoroughly test the hypothesis of the stigonematacean cyanobacterial identity for *P. filiformis*, we combine the microfossil morphology to analyses of its ultrastructure, chemistry and metal distribution. These diagnostic features include ultrastructural criteria such as the structure of cell walls or the possible presence of thylakoids and their arrangement[19,44,45]; and chemical signatures such as geoporphyrins interpreted as degraded chlorophyll or hemes found in bitumen and derived from cyanobacteria[10] or found in microfossils and derived from algae[46] or possible sunscreen pigments unique to cyanobacteria, if they are preserved in the fossil record.[47–49] Other biopolymers may also support a taxonomic identity, such as the presence of polysaccharides in sheath, but they are not unique to these bacteria.

Here, we first test the hypothesis of a photosynthetic metabolism by analyzing the metal distribution in intracellular inclusions (ICIs) within fossil cells of *P. filiformis* from the 1040–1006 Ma Mbuji-Mayi Supergroup (DRCongo), revealing the preservation of geoporphyrins. We then compare the ultrastructure and chemistry of the microfossils to possible modern cyanobacterial and algal analogues with similar morphology. The combination of these new data strongly supports a cyanobacterial identity for *P. filiformis*, and more precisely, it reveals diagnostic features allowing its taxonomic placement within the Stigonemataceae.[27]

RESULTS

Morphology and morphometry of *P. filiformis*

The studied specimens of *Polysphaeroides filiformis* from the 1040–1006 Ma Mbuji-Mayi Supergroup are preserved in fine-grained clay-rich layered sediments (shales), as carbonaceous compressions flattened parallel to bedding. They consist of filamentous chains of spheroidal cells surrounded by a common sheath (Figures 1A and 1B). Cells within the sheath display a multiseriate arrangement and are often superimposed implying a multiplane division mode. The cells range between 5 and 29 μm in diameter and may be dispersed or arranged in pairs, tetrads or clusters. Some specimens of *P. filiformis* may be branched and display a true T-type branching (Figure 1B). Cells of *P. filiformis* often include dark brown inclusions, with a diameter ranging from 1 to 7 μm (Figure 1A). These inclusions, called ICIs and found in diverse organic-walled microfossils, have been variably interpreted as remains of condensed cytoplasm, nuclei, or chloroplasts.[50,51] They differ from dark sulfides or oxides present in the sheath and occasionally within cells by their lighter brown color, their ovoid rather than angular shape, and their generally larger size than sulfides and oxides. Raman microspectroscopy confirms their kerogenous composition and syngenicity (Figure S2; Table S3). The measurements of the sheaths, trichomes, cells and ICIs diameters for 30 *Polysphaeroides filiformis* specimens are shown in Table S4.

Characterization of the metal distribution within *P. filiformis*

P. filiformis is often morphologically compared to cyanobacteria, red or green algae (see aforementioned references). To test the hypothesis of a photosynthetic metabolism, we used SR-nanoXRF technique to detect possible metal (Ni) enrichment and SR-μXANES to determine its

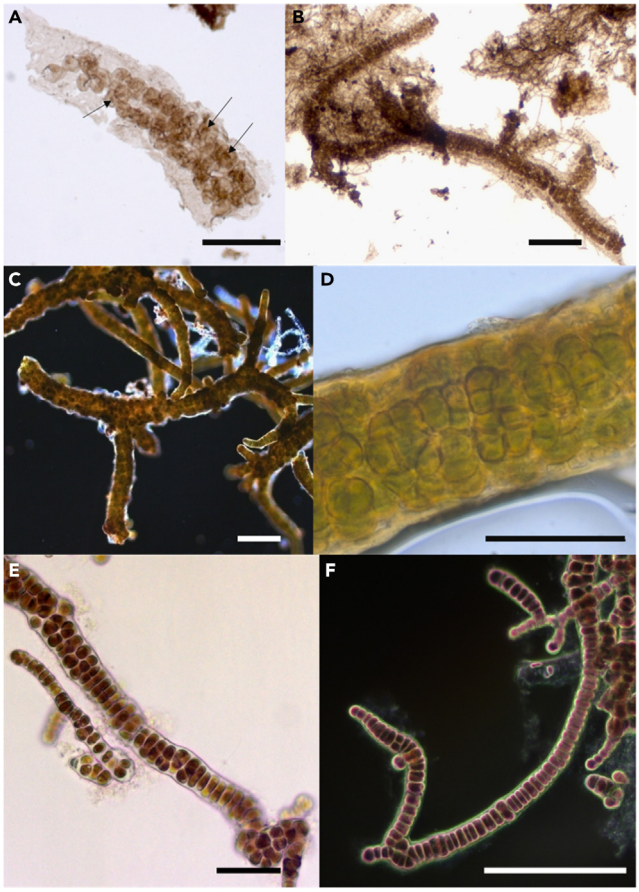

Figure 1. Morphology of the microfossil *Polysphaeroides filiformis* and of modern cyanobacteria and a modern red alga

Microphotographs of *Polysphaeroides filiformis* (A and B), *Stigonema robustum* CBFS-A027 (C), *Stigonema informe* CBFS-A033 (D) and *Bangiopsis franklynottii* CCMP3416 (E and F).

(A) black arrows show ICIs within fossil cells.

(B) True T-type branching of the filament.

(C and F) True T-type branching is visible for all the species.

(E) Unbranched filament of *B. franklinottii* also showing the two types of cells: spherical or flat cells. (Scale bars: A, D, and E = 50 μm; B, C, and F = 100 μm).

configuration (speciation in organic or inorganic molecules). Indeed, during degradation of chlorophylls, Mg is lost early and ultimately replaced by Ni or V.[52,53] In sedimentary environments,[52,54] Ni-porphyrins mostly derive from chlorophylls and their presence was recently demonstrated within a microfossil using this approach.[46] We also analyzed other elements of possible diagenetic or metabolic interests. SR-nanoXRF mapping showed the presence of Fe>>Ni>Cu, Co, Zn> S, Br within *Polysphaeroides filiformis* structures (sheath, cell walls and ICIs) (Figure 2). All elements are found in the sheath, whereas only Br, Ni, Fe, and S are also distributed in cell walls (Figures 2B, 2C, 2G, and 2I). Moreover, Br, Ni, and Fe have higher signal intensities in the folds and at the edges of the cells due to the substantial thickness of these zones. ICIs are particularly enriched in Ni and Co compared to the sheaths and the cell walls (Figures 2C and 2D), whereas V is not enriched in ICI but shows a homogeneous distribution pattern linked to diagenesis, like Zn (see Figures S5, S6, and S7). Indeed, Ni is enriched 5 and 27 times more in the ICIs than in the cells walls and 11 to 54 times more concentrated in ICIs than in the sheath (Table S8). Concentrations of Ni were measured in ICIs, ranging from 2.51 pM to 36.81 pM (Table S9). Co has a signal 6 to 29 times higher in the ICIs than in the cell walls and 48 times higher compared with the sheath. In some specimens, the ICIs can also show a slight enrichment in Cu compared to the sheath (Figure 2F). Finally, when present in the ICIs, Fe is generally present as small hotspots, often correlated with sulfur, suggesting that these hotspots could be sulfides. These sulfides can also be enriched in Ni, Co, and Cu.

Speciation of Ni in ICIs

Nickel K-edge μXANES spectra (Figure 3) exhibit a distinct doublet feature on the white line at ~8352 and ~8360 eV (c and d), with a shoulder at 8340 eV (b) and a discrete pre-edge feature at 8332 eV (a). The ICIs spectra differ from Ni atoms randomly distributed in graphitic carbon vacancies[55] or Ni linked to humate ligands.[56] These spectral shape are consistent with Ni-porphyrin standards such as Ni-octaethyl porphyrin

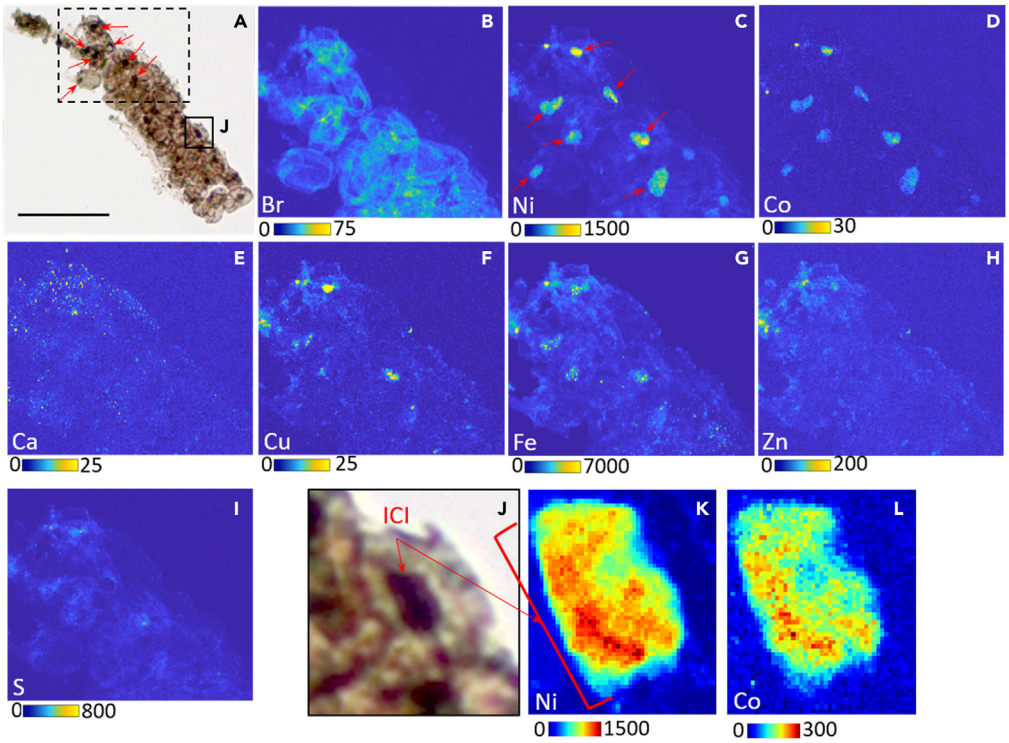

Figure 2. Distribution of elements in the microfossil *Polysphaeroides filiformis*

(A) Microphotograph (Scale bar = 50 μm) of the studied specimen with a dashed box that corresponds to the selected area where SR-nanoXRF maps were acquired. Red arrows show ICIs within several cells.

(B–I) SR-nanoXRF maps of Br, Ni, Co, Ca, Cu, Fe, Zn, and S, obtained at synchrotron ESRF (pixel: 300 nm, 250 ms/px). (B) shows the enrichment of Br in cell walls. (C and D) show the specific enrichment of Ni and Co, respectively, in ICIs. (C) shows, with red arrows, the same ICIs pointed in (A). (G) shows the enrichment of Fe in *P. filiformis* and highlights that Fe is mainly present as hotspots in ICIs and not homogeneously such as Ni and Co.

(J) Zoom on a single cell from *P. filiformis* ((J) in microphotograph (A)). The brown cell contains a black structure (the ICI – red arrow) in the center.

(K and L) SR-nanoXRF maps of Ni and Co in the ICI (red bracket) within the cell (J). Maps in (K) and (L) were also obtained at synchrotron ESRF (pixel: 100 nm, 500 ms/px). Color scales correspond to the number of counts for each map. The darker red corresponds to the higher number of counts and the darker blue is the lower number of counts. For more results, see Figures S5–S7, S10, and S11.

[NiOEP] and Ni-tetraphenyl porphyrin [NiTPP] previously reported Ni K-edge XANES spectra where Ni(II) occurred in porphyrinic square-pyramidal N coordination in asphaltene and cokes[57,58] and in the algal fossil *Arctacellularia tetragonala*.[46] The difference between the ICI and the porphyrin standard spectra (position of the shouldering (a), change of the relative intensities and the broadening of the white line bands (c and d), [Figure 3]) can be explained by the incorporation of the porphyrins in a kerogen network.[46,56,57] The Linear Combination Fitting (LCF) of the Ni K-edge XANES spectra shows that the proportion of Ni in tetrapyrrole species varies between 50% and 90% in the different ICIs (Table S12), whereas the remaining percent in the ICIs are explained by inorganic Ni possibly as NiO and Ni_2S_3. As shown by the sulfur map (Figure 3), S is very low in point 1 while it seems to be more concentrated in point 2 and associated with Fe, possibly suggesting the possible presence of small sulfides in the ICI even if not evidenced with Raman spectroscopy. The SR-μXANES analysis was performed in the part of the ICI where S and Fe were the lowest but still with high Ni, but a contribution of these nano-sulfides to the SR-μXANES spectra cannot completely be excluded. These results are still significant in showing that an important fraction of Ni is contained in tetrapyrrole moieties in the ICIs.

Morphology and morphometry of possible modern analogues

Fossils were then compared to modern photosynthetic organisms with analogous morphology (Figure S15), including three species of modern *Stigonema* spp. showing a similar filamentous morphology consisting of chains of rounded cells surrounded by a common sheath (Figures 1C and 1D). Filaments are all multiseriate and display a true T-type branching (Figure 1C). The cell diameter ranges between 8.6 and 25.8 μm in *S. robustum* (n = 25), between 8.1 and 18.9 μm in *S. turfaceum*, and between 5.5 and 14.6 μm in *S. informe* (Figure 1D; Table S4).

Comparison was also made with *Bangiopsis franklynottii* CCMP3416, a filamentous branching red alga embedded and surrounded by mucilage described as a polysaccharidic matrix by West and colleagues (2014).[60] Filaments are composed of cells that can have either a flattened shape (Figure 1F), or an oval shape (Figure 1E). Flattened cells are stacked one above the others forming a uniseriate trichome (Figure 1F), while ovoid cells are arranged into rather disorganized multiseriate filaments (Figure 1E), forming aggregates in a polysaccharide

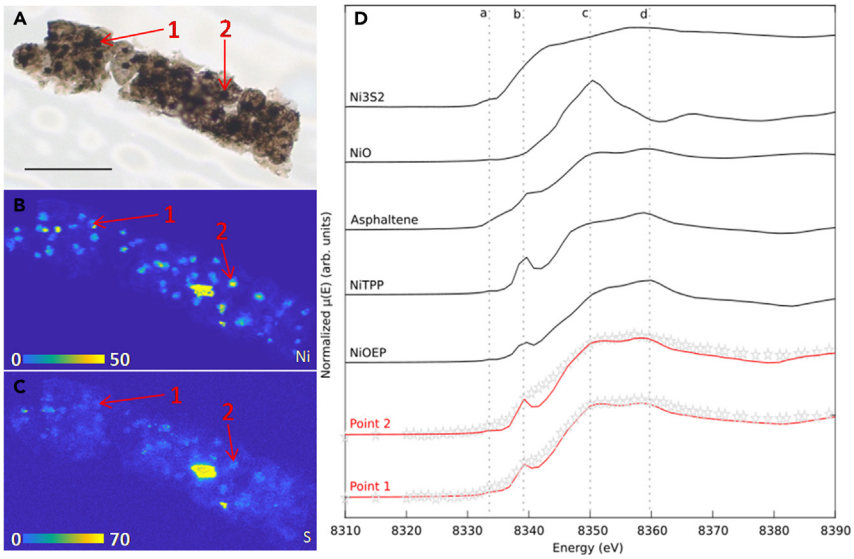

Figure 3. XANES analyses highlighting the presence of Ni-tetrapyrroles in ICIs of *Polysphaeroides filiformis*

(A) Microphotograph of *P. filiformis* (Scale bar: 50 μm).

(B and C) SR-nanoXRF maps, obtained at synchrotron Soleil (pixel 300 nm, 200 ms/px), showing the specific enrichment of Ni (B) and S (C) in ICIs and spots where XANES spectra were obtained with a low iron content (red arrows).

(D) μXANES spectra acquired at SLS, at the Ni K-edge obtained on 2 ICIs (gray stars), red lines correspond to the linear combination fitting of the two points. Black lines correspond to XANES spectra obtained for two Ni-porphyrins (Ni(II)-tetraphenylporphine (NiTPP) and Ni(II)-octaethyporphine (NiOEP)),[57] asphaltene,[59] NiO and Ni_3S_2 standards. The fitting for Points 1 and 2 was made with standards showing molecular heterogeneities between them. This, coupled with incorporated tetrapyrroles moieties in the kerogen, causes the differences between fitting and data lines. The color scale bar corresponds to normalized counts. Color scales in B and C correspond to the number of counts for each map. The most yellow corresponds to the higher number of counts and the bluest is the lower number of counts. For more results, see Figures S13 and S14.

matrix, due to their cell divisions in various planes.[60] Cells dimensions are between 4.7 × 6.2 μm and 12.1 × 13.9 μm (Figure 1; Table S4). Filaments of *B. franklynottii* CCMP3416 form true T-type branching (Figure 1F).

Ultrastructure and fine morphology

SEM imaging of *P. filiformis* shows a granular appearance of the sheath (Figures 4A and 4B), with irregular perforations probably due to mineral imprints or other taphonomic processes (Figure 4C), as well as some folding (Figure 4C), confirming the flexibility of the thin organic sheath.

The ultrastructure of unstained *P. filiformis* specimens embedded in resin was observed in transversal ultrathin sections with transmission electron microscopy (TEM). *P. filiformis* sheath is three-layered and varies in thickness along the section from 40 to 90 nm (Figure 4D). It consists of electron-dense outer and inner layers of ~20 nm in thickness and sandwiching a thicker electron-lucent layer (Figure 4D). Along the TEM section, both sides of the sheath can be merged (Figure 4E). In the internal space, well-defined oval structures, closed at both ends, are observed (Figure 4F). Their walls are bilayered with an external electron-dense layer and an internal electron-lucent layer (Figure 4F). These structures are ~45 nm thick and ~2 μm long, in agreement with the cell dimensions of *P. filiformis* (Table S4; Figures 1A and 1B), suggesting that these structures may correspond to flattened cells preserved compressed within the internal space between both sides of the sheath. Flattening of the microfossil can be asymmetrical, one side of the sheath appearing thicker than the other one (Figure 4G).

The modern cyanobacterial analogue *S. robustum* CBFS-027 was fixed, stained, and embedded in resin, and sectioned transversally by ultramicrotomy. TEM observations reveal a three-layered ultrastructure for the sheath (Figures 4H and 4I). Both external and internal layers are electron-dense and thinner than the median electron-lucent layer (Figure 4I). The overall sheath thickness ranges between 176 and 550 nm. Cells are visible and are embedded within a gel-like electron-lucent matrix, which is itself surrounded by the sheath (Figure 4I).[61] Moreover, an individual envelope is visible around cells (Figure 4I). This special envelope may appear around cells in old parts of filaments.[62] The cells show a bilayered cell wall with a thickness ranging from 65 to 214 nm (Figure 4J). The bilayered cell wall comprises an electron-dense external layer and an electron-lucent inner layer. Numerous cells and their cytoplasmic content are collapsing and shrinking, probably due to dehydration and death of the filaments (Figure 4I). Interestingly, this illustrates how the ICIs observed in microfossil cells may have formed. Collapse of cyanobacteria cell content has been previously documented in fossil and experimental studies.[63,64]

The red alga *B. franklynottii* CCMP3416 shows a quite complex cell wall ultrastructure. The cell wall has a thickness between 262 and 525 nm, and is laminated (Figures 4K and 4L). It is surrounded by a thinner (~40 nm thick) and trilaminar outer layer (Figures 4K and 4L),

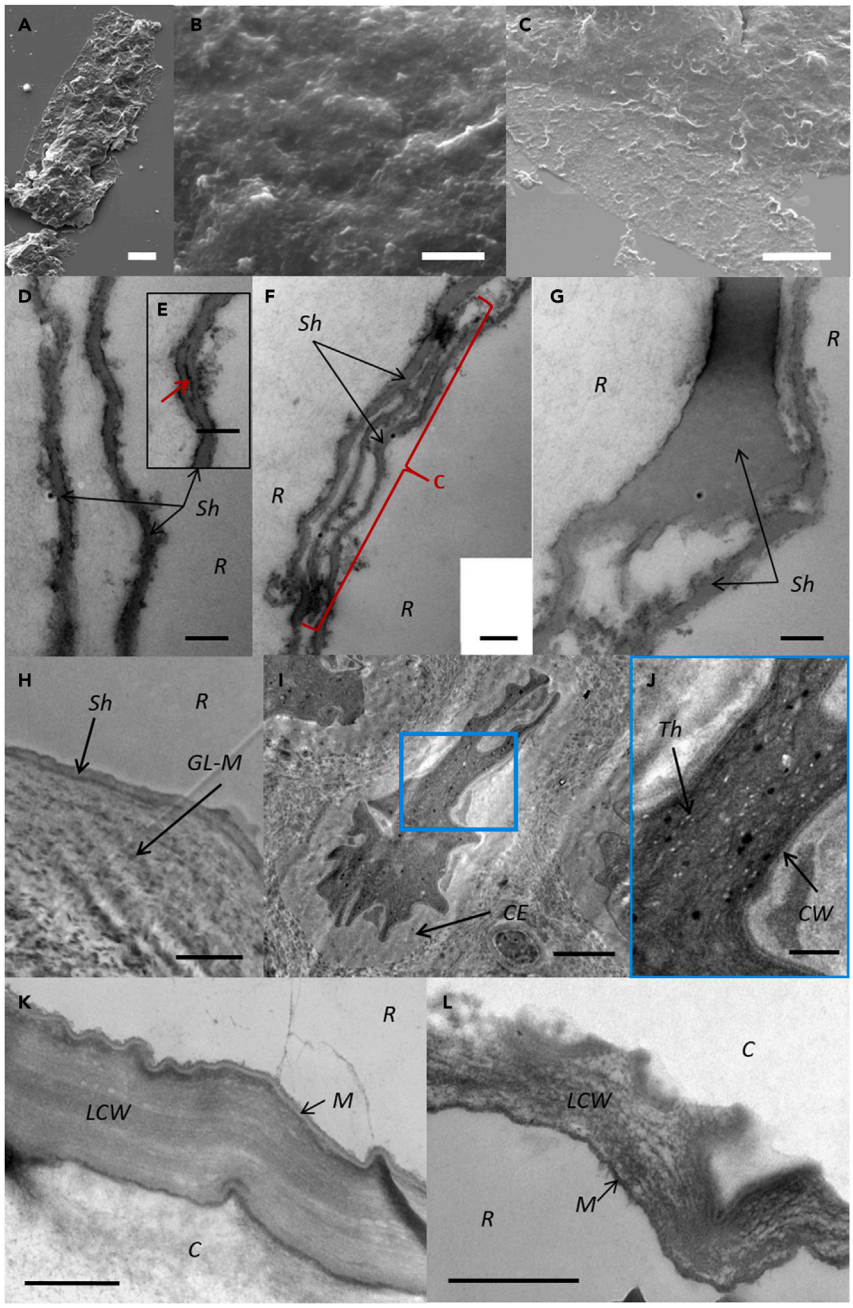

Figure 4. Ultrastructure of the microfossil *Polysphaeroides filiformis* and of a modern cyanobacterium and a modern red alga

SEM (A–C) images of *Polysphaeroides filiformis* and TEM (D–G) images of *P. filiformis*, *Stigonema robustum* CBFS-A027 (H–J) and *Bangiopsis franklynottii* CCMP3416 (K and L).

(A) *P. filiformis* showing a thickened median part surrounding the filaments inside the sheath and laterally thinner flattened parts of the sheath.

(B) Granular appearance of the sheath.

(C) Taphonomic folds and holes in the sheath. Ultrastructure of *Polysphaeroides filiformis* (D–G), *Stigonema robustum* CBFS-A027 (H–J) and *Bangiopsis franklynottii* CCMP3416 (K and L).

(E) Red arrow shows the intracellular space as a black line between the two sides of the sheath that have merged.

(F) The red curly bracket shows a cell within the two sides of the sheath in *P. filiformis*.

(G) The variable thickness of the two sides of the sheath of *P. filiformis* is visible, due to variable compression or tangential sectioning.

(H) *Stigonema robustum* CBFS-A027 has a thin sheath enveloping a thick gel-like matrix in which a cell is embedded (I). The cell has its own cell wall (J).

Figure 4. *Continued*

(K and L) multilayered laminated cell wall with an outer mucilage (polysaccharidic) layer of *Bangiopsis franklynottii* CCMP3416. Letters correspond to: Resin (*R*), Sheath (*Sh*), Cell (*C*), Cell envelope (CE), Cell wall (*CW*), Gel-like matrix (*G-LM*), Laminated cell wall (*LCW*), Mucilage (*M*). (Scale bars: A = 20 μm; B = 1 μm, C = 10 μm, D–G = 200 nm; H and I = 2 μm; J–L = 500 nm).

with two electron-dense layers surrounding a median electron-lucent layer (Figure 4K). This outermost trilaminar layer probably corresponds to the polysaccharide matrix visible in transmitted light (Figure 1E) and described in West et al. (2014).[60]

Molecular composition using FT-IR microspectroscopy

Representative spectra for the red alga *B. franklynottii* CCMP3416, cyanobacteria *S. ocellatum* SAG48.90, sheaths of scytonemin-producing *Calothrix* sp. BCCM/ULC003, and the fossil *P. filiformis* are shown on Figure 5. The band assignments were made based on the second derivative of each spectrum and summarized in Table S16.

The spectrum of *P. filiformis* first shows a broad absorbance located in the region 3,500 and 3,000 cm^{-1}, corresponding to various OH vibrations, mainly attributed to alcoholic OH, phenolic OH and/or carboxylic OH.[65–67] Bands assigned to the stretching of aliphatic bonds CH_2 and CH_3 are present around 2,850 cm^{-1}, 2,918 cm^{-1}, and 2,965 cm^{-1}. Other modes of vibrations of CH_2 and CH_3 are found at ~1,432 cm^{-1} and ~1,466 cm^{-1}, respectively.[65,66] A small shoulder is present around 1,730 cm^{-1} and is interpreted as C=O carbonyl stretching.[65] Another absorption area is observed between 1,150 cm^{-1} and 1,000 cm^{-1}, corresponding to the vibrations of C-O-C, C-O, C-C functional groups.[65] Bands present between 900 cm^{-1} and 600 cm^{-1} correspond to a mixed type of vibrations, notably aromatic CH out of plan deformation.[65,67,68] Similarly, two bands corresponding to the vibration of aromatic C-C ring stretch and conjugated C=O are observed at 1,594 cm^{-1} and at 1,671 cm^{-1}, respectively. Bands at 1,534 cm^{-1} and 1,625 cm^{-1} could be interpreted as vibration of aliphatic COOH and aromatic C=C, respectively, although vibration of C=CH attached to cyclopentene ring can also be found at the wavenumber of 1,625 cm^{-1} and aliphatic COOH at 1,532 cm^{-1}.[67] Moreover, small bands at 1,625 cm^{-1} and 1,671 cm^{-1} may form duet corresponding to conjugated C=O.[65] However, this region may also reveal bands assigned to amides I (e.g., study by Loron et al.[69]).

In the representative spectra of the modern organisms, a first marked region is represented by the broad band corresponding to diverse OH vibrations between 3,000 cm^{-1} and 3,700 cm^{-1}. Bands present around 2,859 cm^{-1}, 2,887 cm^{-1}, and 2,929 cm^{-1} are visible and correspond to the stretching of CH_2 and CH_3 aliphatic bonds. Bands located around 1,633 cm^{-1}, 1,545 cm^{-1}, and 1,319 cm^{-1} are assigned to amide I, amide II and amide III vibrations, respectively.[66] The region between 1,150 cm^{-1} and 1,000 cm^{-1} contains bands assigned to C-O-C, C-C, and C-O stretching of polysaccharides. Specifically in *B. franklynottii* CCMP3416 spectrum, the band found at 1,206 cm^{-1} corresponds to the vibration of sulfate esters.[70] For the three spectra, bands found below 830 cm^{-1} correspond to CH out-of-plane bending vibrations and bonds found in DNA. However, the spectrum of *B. franklynottii* CCMP3416 shows a band at 928 cm^{-1} and a shoulder at 1,074 cm^{-1} that are assigned to C-O vibrations of the 3,6-anhydro-bridge of galactose.[70] We also recognize some of the bands possibly associated with the pigment scytonemin[47,71] present in *Calothrix* sp. BCCM/ULC003 (see Table S16 for more details) and absent in *S. ocelatum* SAG 48.90.

DISCUSSION

Evidence of a photosynthetic metabolism in *P. filiformis*

SR-nanoXRF and SR-μXANES analyses showed that nickel is enriched in the ICIs and is contained in tetrapyrrolic moieties bound to the kerogen forming the ICIs. This indicates the presence of degraded chlorophyll in *P. filiformis* and, thus, its metabolic ability to perform photosynthesis. Similar observations and interpretations were made for another microfossil, *A. tetragonala*, from the same microfossil assemblage of the Mbuji-Mayi Supergroup.[46] The latter microfossil was interpreted as an alga, based on the combined evidence of its morphology, ultrastructure and metal distribution. Geoporphyrins are the result of chlorophyll degradation.[52,54] However, tetrapyrrole nuclei are present in numerous bacterial cofactors and hemes (e.g., cytochrome *c* oxidase, cytochrome P450, and cobalamin B12).[72–74] Nevertheless, the high Chl:heme ratio (~10^5:1) present in photosynthetic cells suggests that the geoporphyrins preserved in the geological record are most likely derived from the photosynthetic pigment chlorophyll.[75,76] In addition to the fossil record of porphyrins in Proterozoic bitumen[10] or in fossil alga[46] evidencing their preservation in diagenetic to low-grade metamorphism temperatures (90°C–200°C), experiments on isolated porphyrins show they can withstand temperatures as high as 250°C.[77]

Morphology and morphometry

Because *P. filiformis* was a photosynthetic microorganism, modern photosynthetic microorganisms with a similar complex morphology were selected to further pinpoint the taxonomic identity of the microfossils. *P. filiformis* displays morphological traits (true branching, multiseriate filaments, cellular division in several planes, multilayered sheath and cell walls) with a complexity and dimensions unknown in other photosynthetic bacteria. Moreover, anoxygenic photosynthetic bacteria belonging to purple bacteria, green sulfur bacteria and heliobacteria do not form multiseriate filaments embedded in a common branching sheath.[78,79] Despite they may be filamentous, such as the best-known species *Chloroflexus aurantiacus*,[78] they do not present branching.[78–80] The morphology of *P. filiformis* is most consistent with the morphology of cyanobacterial genus *Stigonema*. Indeed, modern *Stigonema* spp. also have cells arranged into multiseriate and uniseriate filaments,[81] surrounded by a prominent sheath with similar dimensions to *P. filiformis* (Figure 1; Table S4). Moreover, they also show a true T-type branching (Figure 1C). Eukaryotic red, green, golden-brown, and brown algae may also display multicellular filaments with true

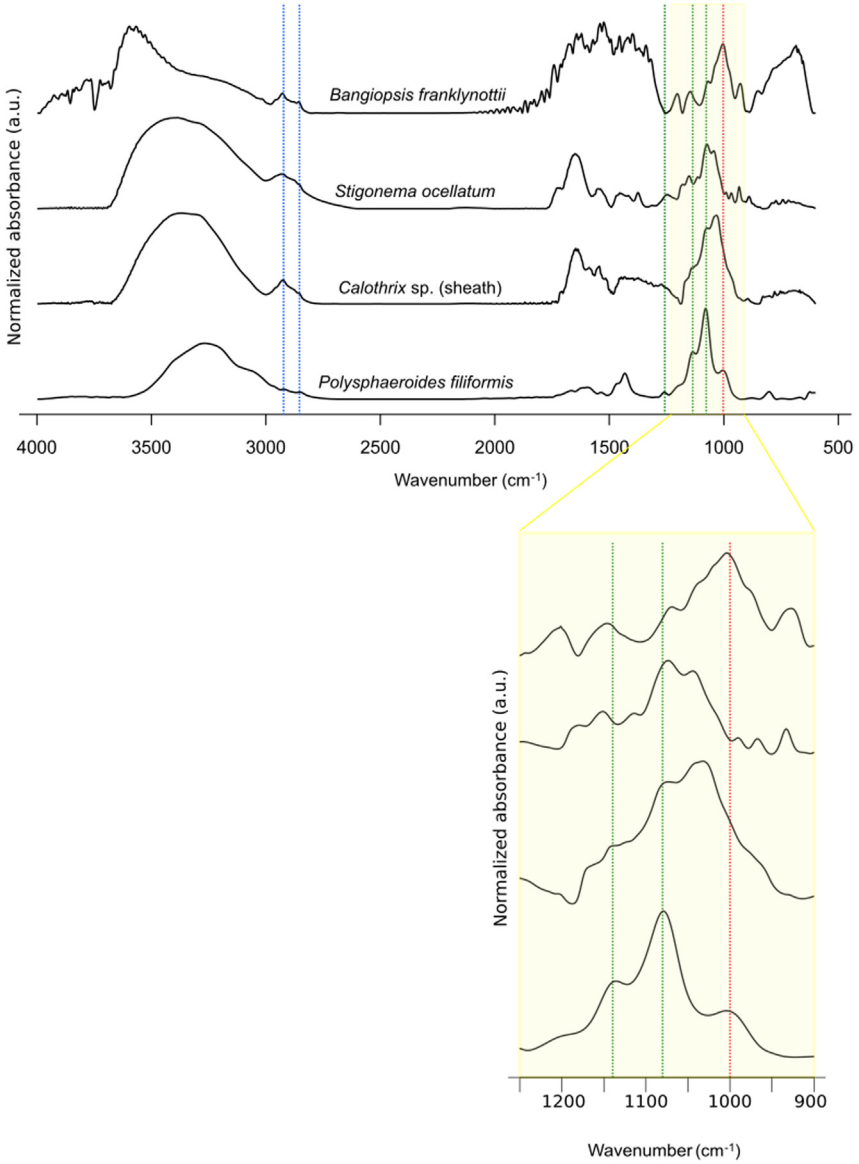

Figure 5. Representative FT-IR spectra of the studied fossil, *Polysphaeroides filiformis*, and modern specimens of *Calothrix* sp. BCCM/ULC003 (sheath), *Stigonema ocellatum* SAG48.90 and *Bangiopsis franklynottii* CCMP3416

The bands represented by the green lines are more similar between *P. filiformis* and the two cyanobacteria in contrast to *B. franklynottii*, which also shows these bands but with a smaller intensity. The red line represents the major band of the polysaccharidic region of *B. franklynottii* that is more intense compared to bands with green lines. This red line, although also visible on *P. filiformis* spectrum, is less intense than in *B. franklynottii* CCMP3416. There is an inversion between the major bands of the polysaccharidic region of *P. filiformis* and modern cyanobacteria versus *B. franklynottii* CCMP3416. These observations suggest a closer similarity between *P. filiformis* and the studied cyanobacteria and a similar polysaccharidic composition for the fossil sheath to sheaths of the two modern cyanobacteria (*Calothrix* sp. and *S. ocellatum* SAG48.90). The blue lines represent bands related to aliphatic CH_2 and CH_3. The green and red lines represent the bands related to C-O-C, C-O, C-C functional groups.

branching.[60,82–84] Among red algae, *B. franklynottii* is the taxon with a morphology most like *P. filiformis*.[60] It is a true-branching red alga that may show uniseriate and multiseriate filaments and cell division in several planes. However, two shapes of cells were observed (flattened and oval), which are not present in *P. filiformis*. Branching in *B. franklynottii* seems to occur more frequently close to the holdfast of this benthic alga[60] (Figure 1F). Other red algae show some similarities to *P. filiformis* in morphology, such as *Bangia* sp., *Polysiphonia* sp., or *Neosiphonia* sp.[85–87] However, *Bangia* shows unbranched filaments and longitudinal division forming wedge-shaped cells and a holdfast, unlike *P. filiformis*.[85,86] *Polysiphonia* and *Neosiphonia* have branched filaments with large rectangular cells (longer than wide) and large spherical tetrasporangia, while *P. filiformis* cells are spherical and much smaller, ranging from 5 to 28 μm in diameter in *P. filiformis*, compared to 21.5 to 96.3 μm long and 16.8 to 63.3 μm wide in *Polysiphonia morrowii*.[87,88] Among green algae, the Chaetophoraceae family includes

multicellular branched filamentous clades, such as *Ulothrix*.[87] However, filaments are exclusively uniseriate. *Ulva flexuosa* (Ulvaceae) is a branched green alga but has rectangular to polygonal cells unlike *P. filiformis*.[87] Finally, branched filaments are also present in brown algae, but most of them are uniseriate except for the genus *Sphacelaria*.[83] Although Sphacelariales have true branching, they form rectangular cells that are larger (38 × 14 μm or 24 × 10 μm depending on the species) than cells of *P. filiformis*.[89] So far, branching in *P. filiformis* is rarely observed and only in the DRC fossil assemblage at our knowledge. *Stigonema* spp. and *B. franklynottii* are both forming thalli composed of branching filaments erected above the sediment surface.[60,62]

Ultrastructure

Remarkably, *P. filiformis* has a sheath composed of three layers, as also observed in the modern cyanobacterium *S. robustum* CBFS-A027. In *P. filiformis*, SEM observations clearly show the thin flattened sheath with a thicker and wider central portion where it envelops the filaments (Figures 4A and 4D). Moreover, rare outgrowths of the sheath toward the internal space are observed along the ultra-thin section (Figure 4G) and could correspond to thickening of the sheath between cells, as observed in modern sheathed filamentous cyanobacteria.[90] In addition, the cell walls in both *P. filiformis* and *S. robustum* CBFS-A027 seem similarly bilayered on TEM images, although cell walls of cyanobacteria are gram-negative walls and consist of four thin layers.[61] This bilayered rather than quadri-layered wall structure might be due to the compression of the fossil *P. filiformis* in shales and of the modern *Stigonema robustum* preserved dry in a herbarium. Both differ strongly from the cell wall of *B. franklynottii*, which is thicker, rather complex and laminated, unlike in *P. filiformis*. Therefore, despite the similarities in metabolism and some morphological features of *P. filiformis* and *B. franklynottii* CCMP3416, their ultrastructural features clearly differ.

Biopolymer composition

Analysis of the major bands in the carbohydrates region shows a preferential preservation of polysaccharides in *P. filiformis*. Its FT-IR spectrum indicates the possible presence of aldose type deoxy sugar such as ribose 5-phosphate according to bands that could potentially be assigned to carbonyl and enediol bands position at 1,730 cm^{-1} and 1,671 cm^{-1},[91] moreover the presence of bands affiliated to both carboxylic acid and carbonyl suggests the presence of uronic acids (Table S16). However, the relative bands intensities at 1,002 and 1,079 cm^{-1} in *P. filiformis* and the modern cyanobacteria between 1,032 and 1,074 cm^{-1} show opposite trends compared to those of red alga *B. franklynottii* CCMP3416 spectrum at 1,006 and 1,074 cm^{-1} (Table S16; Figure 5). This observation suggests that the carbohydrates region of *P. filiformis* spectrum is more consistent with those of a modern polysaccharidic cyanobacterial sheath (Figure 5).[92] Moreover, the spectrum of *B. franklynottii* CCMP3416 presents a bond assigned to galactans at 1,206 cm^{-1}. It also shows a band at 928 cm^{-1} and a shoulder at 1,074 cm^{-1} that are both assigned to vibrations of the 3,6-anhydrogalactose, a sugar unique to red algae.[70,93,94] These bonds are absent in *P. filiformis* spectrum, except the band at 1,079 cm^{-1} but it is present as a strong band and not as a shoulder and is interpreted as C-O deformation (Table S16).[70,95] Although the exact structure of the sugars of the fossilized sheath of *P. filiformis* cannot be evaluated with FT-IR, this interpretation resonates with the composition of modern heterocytous filamentous cyanobacteria extracellular polymeric substances, which are often dominated by uronic acids and deoxy sugars.[96] In addition to polysaccharides, modern *Stigonema* spp. sheaths may sometimes contain the pigment scytonemin but this is not conclusive in the spectrum of *P. filiformis*. Thus, despite changes underwent during diagenesis, the molecular composition of *P. filiformis* revealed by FT-IR spectroscopy appears more similar to that of polysaccharidic sheaths of modern scytonemin producing-*Calothrix* BCCM/ULC003 and unpigmented *S. ocellatum* SAG48.90.

Concentration of Ni-porphyrins in *P. filiformis*

In *P. filiformis*, we estimated the concentration of Ni-tetrapyrroles in the ICIs between 2.51 pM and 36.81 pM (Table S9). This tetrapyrrole concentration is lower than the chlorophyll concentration in modern cyanobacteria (e.g., 2.18 mM in *Anabaena variabilis* UTEX B377, 2.46 mM in *Microcystis aeruginosa* LE-3 and 1.2–2.5 mM in *Synechococcus* sp. WH 7803),[97,98] as expected for 1 Ga old microfossils. Moreover, the tetrapyrrole concentration of *P. filiformis* is also much lower than in *A. tetragonala*.[46] This difference could be explained by the initial cellular distribution of the photosynthetic pigments in cyanobacteria versus eukaryotic algae. Indeed, in cyanobacteria, chlorophylls are stacked in thylakoidal membranes deployed in the cytoplasm of the cells while in algae, the thylakoidal membranes are condensed within an organelle, the chloroplast, which derives from an ancestral cyanobacterial endosymbiont. The presence of chloroplasts protected in decay-resistant eukaryotic algal cell walls may ensure a better storage of degraded chlorophyll in algal cells than in cyanobacterial cells and could explain the difference of preservation rates. In addition, in the marine environment, chlorophyll *a* content increases with cell volume in fractionated phytoplankton.[99]

An exogenic and/or late origin of such bound Ni-geoporphyrins in *P. filiformis* can also be excluded. Indeed, the porphyrins are specifically associated to the ICIs, which are clearly syngenetic, as demonstrated by their distribution, and by the similar Raman spectra compared to the overall fossil Raman spectra (see Figure S2; Table S3). Finally, no evidence for late bitumen covering cell walls or filling the microfossil cavities was reported in the Mbuji-Mayi BIIc6 Formation.[46,100] Thus, the SR-nanoXRF and of the SR-μXANES analyses of Ni distribution in *P. filiformis* ICIs support a photosynthetic metabolism.

Co, Cu, and Br: Other possible elements of interest as metabolic tracers

The metals Co and Cu are also observed in ICIs though with lower signal intensity (Figure 2). Co is nearly always co-located with Ni (Figures 2C and 2D). This co-location could be explained by a co-precipitation of Ni and Co in the disseminated sulfides in the ICIs but also by a

substitution of Ni for Co in the tetrapyrrole structures as the two cations have the same oxidation state and their radii are similar.[101] The rare uncorrelated fraction is not associated with other elements such as Fe or Ca, which suggests that they are not associated in sulfides or neo-fluorides but bound to organic phases. Such absence of correlation between Ni and Co would require organic ligands, which would be distinct from the organic ligands binding Ni and would bind specifically Co over Ni.[102] Interestingly, Co is mainly located in ICIs suggesting a high potential as a metabolic tracer. Indeed, Cobalt is an essential element for life.[103] Cyanobacteria have absolute requirement in Co[104,105] and the cobalt-ligand complexes in cyanobacteria are exceedingly strong.[102] One of the Co-containing molecules present in cyanobacteria has also a tetrapyrrole structure, the cobalamin (vitamin B12). Cobalamin is composed of a corrin ring with a cobalt ion at its center.[103,106] As for chlorophyll, this structure could be stable enough to be potentially preserved in microfossils over long times even if Co-porphyrins are thermodynamically slightly less stable than Ni- and VO-porphyrins.[101] Further analyses are necessary to understand the bearing phase of Co and to use Co as a tracer of Co-bearing molecules, possibly indicative of cyanobacterial affinity or, more generally, of life.

Cu enrichment in fossil ICIs could serve as a potential tracer of photosynthesis or other metabolisms such as respiration in the fossil record. Indeed, enzymatic reactions in modern cyanobacteria often require Cu as a cofactor (e.g., plastocyanin, cytochrome *c*6 oxidase).[107,108] Br mainly occurs in cell walls of *P. filiformis* and is almost absent in the ICIs and sheath. Although its presence may be due to diagenesis,[109] this element may also be found in some biomolecules or be bio-accumulated and may form a wide range of organobromine complexes.[110–112] However, these hypotheses need to be tested by further analyses to determine which specific molecules these metals are possibly bound to.

Implications for the evolution of cyanobacteria

Although previous work[19,32,36] suggested a "Stigonematalean" affinity for *Polysphaeroides filiformis*, this hypothesis remained ambiguous as it was only based on morphology, so convergence with other organisms was possible. Our study establishes *P. filiformis* from the Mbuji-Mayi Supergroup as the first unambiguous Proterozoic stigonematacean microfossil presenting both true-branching and multiseriate cells. This fossil occurrence is half a billion years older than *Rhystigonema obscurum*, a fossil recently found in the Rhynie chert (lower Devonian) and interpreted as a Stigonemataceae.[35] Other microfossils of the terrestrial warm soil and spring environment of the Rhynie Chert, such as *Langiella scourfieldii* and *Kidstoniella fritschii* were also interpreted as possible Stigonemataceae[113] but their taxonomy was emended by Strullu-Derrien et al.[64,] who placed *Kidstoniella fritschii* and *Rhyniella vermiformis* under a single species *Langiella scourfieldii*, interpreted as a nostocalean cyanobacterium from the family Hapalosiphonaceae.[64,113] Although they are true-branched, the taxonomy of these fossil taxa has been emended as their main axis is predominantly uniseriate with some moderately multiseriate parts, while their branches are only uniseriate, these characteristics reflecting the description of Hapalosiphonaceae and not Stigonemataceae.[64]

P. filiformis has a worldwide distribution in Mesoproterozoic and Neoproterozoic successions in Siberia, the East European platform, North China and DRCongo in central Africa. The fossils studied here are preserved in shallow-marine environment of the Mbuji-Mayi Supergroup (DRCongo) with no evidence of fluvial inputs,[42] suggesting Stigonematacean cyanobacteria may have diversified first in marine environments before developing in terrestrial settings. The oldest *P. filiformis* specimens are reported in the Ust'-Il'ya and Kotuikan formations (1483 $\pm$ 10 Ma and 1457 $\pm$ 220 Ma, respectively),[39–41] but these specimens do not show branching, the width of their sheaths is narrower (~9 μm for the Ust'-Il'ya specimens and 12–17 μm for the Kotuikan specimens) and their cell shape (hexagonal) differs from *P. filiformis* from the Mbuji-Mayi Supergroup studied here (Figure 9.13 in a study by Vorob'eva et al[39]). However, the Siberian material also includes one specimen of an unnamed microfossil (Figure 10.10 in a study by Vorob'eva et al[39]), showing multiseriate filaments with spherical cells and surrounded by a common sheath that also has true branching and closely resembles *P. filiformis* from the Mbuji-Mayi Supergroup despite a narrower width of the sheath (14–17 μm), possibly representing the oldest occurrence of this taxon.

Based on the unambiguous interpretation of *P. filiformis* as a stigonematacean, we propose that N-fixing heterocytous cyanobacteria already diversified by 1 Ga. Although we cannot eliminate the hypothesis that early Nostocales did not yet form heterocytes, all know modern nostocales do and this is one of the characters defining the Nostocales. Heterocytous cyanobacteria, previously subdivided into Stigonematales and Nostocales, form a monophyletic clade reclassified as the single order Nostocales based on molecular analyses.[27,114] They have developed specialized cells, the heterocytes, which are anoxic compartments where N_2 fixation occurs.[24,62] Indeed, the nitrogen-fixing enzyme, nitrogenase, is inhibited when the oxygen content in the atmosphere is higher than 2%.[115] Nitrogenase is exclusively found in some prokaryotic organisms, such as members of several bacterial phyla and one phylum of Archaea.[116] A study based on nitrogen isotopes proposed a minimum age of ~3.2 Ga for biological nitrogen fixation using molybdenum-based nitrogenase.[117] The concentration of oxygen in the atmosphere was probably sufficiently low at 3.2 Ga for nitrogenase activity without requiring the evolution of heterocytes.[115] Some authors suggest an origin of heterocytous cyanobacteria to protect nitrogenase enzymes from increasing oxygenation of the early atmosphere[112] between 2.45 and 2.1 Ga,[31] following the GOE, while others propose that heterocytes evolved long after, during the Phanerozoic based on their putative Devonian fossil record. However this Paleozoic record was reassessed as dubious.[64] Indeed, fossil heterocytes are difficult to identify based on morphology alone. Moreover, modern Nostocales do not produce them continuously so they might be rarely preserved. In the Proterozoic fossil record, several microfossils are proposed as potential candidates for heterocytous cyanobacteria. Emblematic examples include microfossils interpreted as possible akinetes (Nostocales), such as *Archaeoellipsoides* and other ellipsoidal microfossils such as *Brevitrichoides* and *Navifusa*.[29–33] However, their interpretation remains ambiguous, as their simple ovoid smooth-walled morphology is also encountered in other clades of microorganisms.[19,33] Other ambiguous microfossils proposed as putative heterocytous cyanobacteria include the genera *Orculiphycus*, *Glenobotrydion*, *Polytrichoides*, *Uroniopsora*, *Filiconstrictosus*, and *Ramivaginalis* (for more details, see review in a study by Sergeev[32]). The microfossil *Anhuithrix magna* was also tentatively interpreted as a heterocytous

cyanobacterium, based on the morphology of larger globose cells irregularly placed within a filament and interpreted as akinetes.[34] Finally, another possible stigonematalean candidate is the unsheathed microfossil *Chlorogloeaopsis*.[32] These microfossils could be investigated using our combined approach to elucidate their identity.

True branching is the latest evolutionary step of morphological complexity to appear.[26] So far, molecular estimations for the age of the appearance of true branching often suggest a late emergence around approximately 0.4–0.6 Ga,[118–120] or an earlier origin around approximately 1.1–1.5 Ga.[2,119,121] The variations observed between the different analyses may be explained by the different datasets, models and constraints used by the authors. The unambiguous interpretation of *P. filiformis* as a stigonematacean cyanobacterium allows now to propose a minimum age for the evolution of true branching at ~1 Ga, implying an earlier diversification of other cyanobacterial clades. *P. filiformis*, as a fossil Nostocales, also provides a minimum age for the appearance of heterocytous cyanobacteria, a more robust constraint compared to the age of the ambiguous microfossil *Archaeoellipsoides*.

Limitations of the study

These are induced by the fact that heterocytes are difficult to identify in microfossils. Moreover, modern Nostocales do not produce them continuously so they might be rarely preserved. Therefore, their emergence can be inferred based on fossils identified as Nostocales although we cannot eliminate the hypothesis that early Nostocales did not yet form heterocytes.

Conclusions

In conclusion, this micro- to nanoscale paleobiological study enabled to firmly identify *Polysphaeroides filiformis* as the oldest unambiguous complex fossil Stigonemataceae known to date, evidenced by the combination of its morphology, ultrastructure, molecular composition and metal distribution (see Table S17 for a summary of results). This work also provides a new calibration point for molecular clocks of ~1 Ga (1040–1006 Ma) for the Stigonemataceae within the Nostocales heterocytous cyanobacteria,[43] pushing back their minimum age by 600 Ma. This age could potentially be extended back in the fossil record with further similar analyses of the older ~1.5 Ga Kotuikan Formation fossil assemblage that includes one unnamed *Polysphaeroides*-like branching specimen.[39] This work also reveals that ICIs may preserve molecular remains of chlorophylls that were here associated with bacterial thylakoidal membranes, and thus here, do not represent nuclei, nor chloroplasts, but shrunken cytoplasm. Thus, the presence of ICIs in fossil cells does not enable to distinguish early eukaryotic from prokaryotic microfossils. Our study illustrates the necessity to conduct micro- to nanoscale multidisciplinary analyses of microfossils in a well-characterized geological context to unambiguously determine their identity and metabolism, and track their evolution further back in time. Finally, this study also proposes perspectives in the analysis of metals within ICIs, such as cobalt and copper, as possible tracers of the early evolution of life and metabolic pathways.

STAR★METHODS

Detailed methods are provided in the online version of this paper and include the following:

- KEY RESOURCES TABLE
- RESOURCE AVAILABILITY
  - Lead contact
  - Materials availability
  - Data and code availability
- EXPERIMENTAL MODEL AND STUDY PARTICIPANT DETAILS
  - Fresh modern cyanobacteria and red alga
  - Geological context and microfossils preparation
- METHOD DETAILS
  - Light microscopy
  - Raman microspectroscopy
  - FT-IR microspectroscopy
  - Synchrotron-based nano X-ray fluorescence (SR-nanoXRF)
  - Synchrotron-based micro X-ray absorption spectroscopy (SR-μXANES)
  - Scanning electron microscopy (SEM)
  - Transmission Electron Microscopy (TEM)
- QUANTIFICATION AND STATISTICAL ANALYSIS

SUPPLEMENTAL INFORMATION

Supplemental information can be found online at https://doi.org/10.1016/j.isci.2024.108865.

ACKNOWLEDGMENTS

We thank the Royal Museum for Central Africa (Tervuren, Belgium) for access to the Kanshi SB13 drillcore and we thank Dr B. K. Baludikay (University of Kinshasa, DRC) for its previous micropaleontological work on the Mbuji-Mayi Supergroup. We thank M. Giraldo, A. Lambion at the Early Life Traces & Evolution–Astrobiology laboratory, S. Smeets at the CAREM platform (University of Liège, Belgium), and C. López-Iglesias and H. Duimel at the Microscopy CORE Lab (University of Maastricht) for technical support. The authors acknowledge Dr J. Kučera (the CBFS herbarium) and Dr T. Hauer from the University of South Bohemia (CZ) for kindly providing *Stigonema* herbaria. The authors also thank the Paul Scherrer Institute, Villigen, Switzerland, the Synchrotron Soleil, Gif-sur-Yvette, and the European Synchrotron Radiation Facility, Grenoble, for provision of synchrotron radiation beamtime at microXAS X05LA, the Nanoscopium and ID16B beamlines, respectively. We thank M.B.J. Lindsay (University of Saskatchewan, Canada) for providing XANES porphyrins spectra. The FRS-FNRS-FWO EOS ET-Home grant 30442502, the ERC Stg ELiTE FP7/308074, the ULiège mini-ARC PUMA project, the BELSPO BRAIN project 188 B2/212/PI/PORTAL, the Marie-Curie Cofund program at the University of Liège, the FNRS CR PROMESS project, and the program CALYPSO PLUS (Synchrotron Soleil) supported this project.

AUTHOR CONTRIBUTIONS

C.F.D., Y.J.L., and E.J.J. designed the research; C.F.D. and Y.J.L. performed optical microscopy; C.F.D., M.C.S., and A.F. performed SEM; C.F.D., E.J.J., M.C.S., Y.C., A.A., A.F., and P.C. performed TEM; C.F.D. and Y.J.L. performed FT-IR microspectroscopy; C.F.D., Y.J.L., and M.C.S. performed Raman microspectroscopy; C.F.D., M.C.S., E.J.J., A.S., K.M., D.G., D.F.S., and R.T.T. performed SR-μXRF and SR-nanoXRF; C.F.D., M.C.S., D.G., and D.F.S. performed SR-μXANES; C.F.D., Y.J.L., and E.J.J. wrote the paper, with contributions from all the authors.

DECLARATION OF INTERESTS

The authors declare no competing interests.

Received: October 25, 2023
Revised: November 29, 2023
Accepted: January 8, 2024
Published: January 11, 2024

REFERENCES

1. Cardona, T., Sánchez-Baracaldo, P., Rutherford, A.W., and Larkum, A.W. (2019). Early Archean origin of photosystem II. Geobiology *17*, 127–150.
2. Fournier, G.P., Moore, K.R., Rangel, L.T., Payette, J.G., Momper, L., and Bosak, T. (2021). The Archean origin of oxygenic photosynthesis and extant cyanobacterial lineages. Proc. Biol. Sci. *288*, 20210675.
3. Holland, H.D. (2002). Volcanic gases, black smokers, and the Great Oxidation Event. Geochem. Cosmochim. Acta *66*, 3811–3826.
4. Eguchi, J., Diamond, C.W., and Lyons, T.W. (2022). Proterozoic supercontinent break-up as a driver for oxygenation events and subsequent carbon isotope excursions. PNAS Nexus *1*, pgac036.
5. Ostrander, C.M., Johnson, A.C., and Anbar, A.D. (2021). Earth's first redox revolution. Annu. Rev. Earth Planet Sci. *49*, 337–366.
6. Raymond, J., and Segrè, D. (2006). The effect of oxygen on biochemical networks and the evolution of complex life. Science *311*, 1764–1767.
7. Sánchez-Baracaldo, P., Bianchini, G., Wilson, J.D., and Knoll, A.H. (2022). Cyanobacteria and biogeochemical cycles through Earth history. Trends Microbiol. *30*, 143–157.
8. Archibald, J.M. (2015). Endosymbiosis and eukaryotic cell evolution. Curr. Biol. *25*, R911–R921.
9. Javaux, E.J. (2021). Eukaryotes, Appearance and Early Evolution of. In Encyclopedia of Astrobiology, M. Gargaud, W.M. Irvine, R. Amils, P. Claeys, H.J. Cleaves, M. Gerin, D. Rouan, T. Spohn, S. Tirard, and M. Viso, eds. (Springer), pp. 1–5. chapter 538-4.
10. Gueneli, N., McKenna, A.M., Ohkouchi, N., Boreham, C.J., Beghin, J., Javaux, E.J., and Brocks, J.J. (2018). 1.1-billion-year-old porphyrins establish a marine ecosystem dominated by bacterial primary producers. Proc. Natl. Acad. Sci. USA *115*, E6978–E6986.
11. Vinnichenko, G., Jarrett, A.J.M., Hope, J.M., and Brocks, J.J. (2020). Discovery of the oldest known biomarkers provides evidence for phototrophic bacteria in the 1.73 Ga Wollogorang Formation, Australia. Geobiology *18*, 544–559.
12. Osterhout, J.T., Schopf, J.W., Williford, K.H., McKeegan, K.D., Kudryavtsev, A.B., and Liu, M.C. (2021). Carbon isotopes of Proterozoic filamentous microfossils: SIMS analyses of ancient cyanobacteria from two disparate shallow-marine cherts. Geomicrobiol. J. *38*, 719–731.
13. Bosak, T., Greene, S.E., and Newman, D.K. (2007). A likely role for anoxygenic photosynthetic microbes in the formation of ancient stromatolites. Geobiology *5*, 119–126.
14. Bosak, T., Knoll, A.H., and Petroff, A.P. (2013). The meaning of stromatolites. Annu. Rev. Earth Planet Sci. *41*, 21–44.
15. Slotznick, S.P., and Fischer, W.W. (2016). Examining archean methanotrophy. Earth Planet Sci. Lett. *441*, 52–59.
16. Golubic, S., and Hofmann, H.J. (1976). Comparison of Holocene and mid-Precambrian Entophysalidaceae (Cyanophyta) in stromatolitic algal mats: cell division and degradation. J. Paleontol. 1074–1082.
17. Hofmann, H.J. (1976). Precambrian microflora, Belcher Islands, Canada: significance and systematics. J. Paleontol. 1040–1073.
18. Hodgskiss, M.S., Dagnaud, O.M., Frost, J.L., Halverson, G.P., Schmitz, M.D., Swanson-Hysell, N.L., and Sperling, E.A. (2019). New insights on the Orosirian carbon cycle, early Cyanobacteria, and the assembly of Laurentia from the Paleoproterozoic Belcher Group. Earth Planet Sci. Lett. *520*, 141–152.
19. Demoulin, C.F., Lara, Y.J., Cornet, L., François, C., Baurain, D., Wilmotte, A., and Javaux, E.J. (2019). Cyanobacteria evolution: Insight from the fossil record. Free Radic. Biol. Med. *140*, 206–223.
20. Huber, A.L. (1985). Factors affecting the germination of akinetes of *Nodularia spumigena* (Cyanobacteriaceae). Appl. Environ. Microbiol. *49*, 73–78.
21. Baker, P.D., and Bellifemine, D. (2000). Environmental influences on akinete germination of *Anabaena circinalis* and implications for management of cyanobacterial blooms. Hydrobiologia *427*, 65–73.
22. Agrawal, S.C. (2009). Factors affecting spore germination in algae. Folia Microbiol. *54*, 273–302.
23. Kaplan-Levy, R.N., Hadas, O., Summers, M.L., Rücker, J., and Sukenik, A. (2010). In "Akinetes: dormant cells of cyanobacteria" in Dormancy and resistance in harsh

environments, E. Lubzens, J. Cerda, and M. Clark, eds. (Springer), pp. 5–27.
24. Haselkorn, R. (1978). Annu. Rev. Plant Physiol. *29*, 319–344.
25. Rippka, R., Stanier, R.Y., Deruelles, J., Herdman, M., and Waterbury, J.B. (1979). Generic assignments, strain histories and properties of pure cultures of cyanobacteria. Microbiology *111*, 1–61.
26. Hammerschmidt, K., Landan, G., Domingues Kümmel Tria, F., Alcorta, J., and Dagan, T. (2021). The order of trait emergence in the evolution of cyanobacterial multicellularity. Genome Biol. Evol. *13*, evaa249.
27. Strunecký, O., Ivanova, A.P., and Mareš, J. (2023). An updated classification of cyanobacterial orders and families based on phylogenomic and polyphasic analysis. J. Phycol. *59*, 12–51.
28. Timofeev, B.V., Hermann, T.N., and Michailova, N.S. (1976). Mikrofitofossilii Dokembria, Kembriaiordovika (Microphytofossils of the Precambrian, Cambrian and Ordovician) (Scientific Institute of Precambrian Geology and Geochronology), p. 106. p [in Russian].
29. Golubic, S., Sergeev, V.N., and Knoll, A.H. (1995). Mesoproterozoic Archaeoellipsoides: akinetes of heterocystous cyanobacteria. Lethaia *28*, 285–298.
30. Amard, B., and Bertrand-Sarfati, J. (1997). Microfossils in 2000 Ma old cherty stromatolites of the Franceville Group. Precambrian Res. *81*, 197–221.
31. Tomitani, A., Knoll, A.H., Cavanaugh, C.M., and Ohno, T. (2006). The evolutionary diversification of cyanobacteria: molecular–phylogenetic and paleontological perspectives. Proc. Natl. Acad. Sci. USA *103*, 5442–5447.
32. Sergeev, V.N., Sharma, M., and Shukla, Y. (2012). Proterozoic fossil cyanobacteria. Palaeobotanist *61*, 189–358.
33. Butterfield, N.J. (2015). Proterozoic photosynthesis–a critical review. Palaeontology *58*, 953–972.
34. Pang, K., Tang, Q., Chen, L., Wan, B., Niu, C., Yuan, X., and Xiao, S. (2018). Nitrogen-fixing heterocystous cyanobacteria in the Tonian period. Curr. Biol. *28*, 616–622.e1.
35. Krings, M. (2021). Stigonema (Nostocales, Cyanobacteria) in the Rhynie chert (Lower Devonian, Scotland). Rev. Palaeobot. Palynol. *295*, 104505.
36. Hermann, T.N. (1990). Organic World One Billion Years Ago (Leningrad: Nauka), p. 50. [in Russian with English summary].
37. Vorob'eva, N.G., Sergeev, V.N., and Knoll, A.H. (2009). Neoproterozoic microfossils from the northeastern margin of the East European Platform. J. Paleontol. *83*, 161–196.
38. Hofmann, H.J., and Jackson, G.D. (1994). Shale-facies microfossils from the Proterozoic Bylot Supergroup, Baffin Island, Canada. J. Paleontol. *68*, 1–35.
39. Vorob'eva, N.G., Sergeev, V.N., and Petrov, P.Y. (2015). Kotuikan Formation assemblage: a diverse organic-walled microbiota in the Mesoproterozoic Anabar succession, northern Siberia. Precambrian Res. *256*, 201–222.
40. Gorokhov, I.M., Kuznetsov, A.B., Semikhatov, M.A., Vasil'eva, I.M., Rizvanova, N.G., Lipenkov, G.V., and Dubinina, E.O. (2019). Early Riphean Billyakh Group of the Anabar uplift, North Siberia: C–O isotopic geochemistry and Pb–Pb age of dolomites. Stratigr. Geol. Correl. *27*, 514–528.
41. Petrov, P.Y., Sharma, M., Vorob'eva, N.G., and Sergeev, V.N. (2019). Facies-stratigraphic distribution of organic-walled and silicified microfossils in the early Billiyakh Basin (Lower Riphean, Anabar Uplift, Siberia). Paleontol. J. *53*, 867–872.
42. Baludikay, B.K., Storme, J.Y., François, C., Baudet, D., and Javaux, E.J. (2016). A diverse and exquisitely preserved organic-walled microfossil assemblage from the Meso–Neoproterozoic Mbuji-Mayi Supergroup (Democratic Republic of Congo) and implications for Proterozoic biostratigraphy. Precambrian Res. *281*, 166–184.
43. François, C., Baludikay, B.K., Debaille, V., Birck, J.L., Limmois, D., Jourdan, F., Baudet, D., Paquette, J.L., Delvaux, D., and Javaux, E.J. (2023). Multi-method dating constrains the diversification of early eukaryotes in the Proterozoic Mbuji-Mayi Supergroup of the DR Congo and the geological evolution of the Congo Basin. J. Afr. Earth Sci. *198*, 104785.
44. Pacton, M., Gorin, G.E., and Fiet, N. (2008). Unravelling the origin of ultralaminae in sedimentary organic matter: the contribution of bacteria and photosynthetic organisms. J. Sediment. Res. *78*, 654–667.
45. Mareš, J., Strunecký, O., Bučinská, L., and Wiedermannová, J. (2019). Evolutionary patterns of thylakoid architecture in cyanobacteria. Front. Microbiol. *10*, 277.
46. Sforna, M.C., Loron, C.C., Demoulin, C.F., François, C., Cornet, Y., Lara, Y.J., Grolimund, D., Ferreira Sanchez, D., Medjoubi, K., Somogyi, A., et al. (2022). Intracellular bound chlorophyll residues identify 1 Gyr-old fossils as eukaryotic algae. Nat. Commun. *13*, 146–148.
47. Lepot, K., Compère, P., Gérard, E., Namsaraev, Z., Verleyen, E., Tavernier, I., Hodgson, D.A., Vyverman, W., Gilbert, B., Wilmotte, A., and Javaux, E.J. (2014). Organic and mineral imprints in fossil photosynthetic mats of an East-Antarctic lake. Geobiology *12*, 424–450.
48. Storme, J.Y., Golubic, S., Wilmotte, A., Kleinteich, J., Velázquez, D., and Javaux, E.J. (2015). Raman characterization of the UV-protective pigment gloeocapsin and its role in the survival of cyanobacteria. Astrobiology *15*, 843–857.
49. Lara, Y.J., McCann, A., Malherbe, C., François, C., Demoulin, C.F., Sforna, M.C., Eppe, G., De Pauw, E., Wilmotte, A., Jacques, P., and Javaux, E.J. (2022). Characterization of the Halochromic Gloeocapsin Pigment, a Cyanobacterial Biosignature for Paleobiology and Astrobiology. Astrobiology *22*, 735–754.
50. Pang, K., Tang, Q., Schiffbauer, J.D., Yao, J., Yuan, X., Wan, B., Chen, L., Ou, Z., and Xiao, S. (2013). The nature and origin of nucleus-like intracellular inclusions in Paleoproterozoic eukaryote microfossils. Geobiology *11*, 499–510.
51. Carlisle, E.M., Jobbins, M., Pankhania, V., Cunningham, J.A., and Donoghue, P.C.J. (2021). Experimental taphonomy of organelles and the fossil record of early eukaryote evolution. Sci. Adv. *7*, eabe9487.
52. Treibs, A. (1936). Chlorophyll and haemin derivatives in organic minerals. Angew. Chem. *49*, 682–686.
53. Tahoun, M., Gee, C.T., McCoy, V.E., Sander, P.M., and Müller, C.E. (2021). Chemistry of porphyrins in fossil plants and animals. RSC Adv. *11*, 7552–7563.
54. Callot, H.J., Ocampo, R., and Albrecht, P. (1990). Sedimentary porphyrins: Correlations with biological precursors. Energy Fuels *4*, 635–639.
55. Jiang, K., Siahrostami, S., Zheng, T., Hu, Y., Hwang, S., Stavitski, E., Peng, Y., Dynes, J., Gangisetty, M., Su, D., et al. (2018). Isolated Ni single atoms in graphene nanosheets for high-performance CO 2 reduction. Energy Environ. Sci. *11*, 893–903.
56. Xia, K., Bleam, W., and Helmke, P.A. (1997). Studies of the nature of binding sites of first row transition elements bound to aquatic and soil humic substances using X-ray absorption spectroscopy. Geochem. Cosmochim. Acta *61*, 2223–2235.
57. Nesbitt, J.A., Lindsay, M.B., and Chen, N. (2017). Geochemical characteristics of oil sands fluid petroleum coke. Appl. Geochem. *76*, 148–158.
58. Nesbitt, J.A., Robertson, J.M., Swerhone, L.A., and Lindsay, M.B.J. (2018). Nickel geochemistry of oil sands fluid petroleum coke deposits, Alberta, Canada. Facets *3*, 469–486.
59. Lytle, F.W. (1983). Data from "Cold Lake Asphaltene V. And Ni X. A. S. Spectra." (International X-ray Absorption Society XAFS Database).
60. West, J.A., de Goër, S.L., and Zuccarello, G.C. (2014). A new species of *Bangiopsis: B. franklynottii* sp. nov. (Stylonematophyceae, Rhodophyta) from Australia and India and comments on the genus. ALGAE *29*, 101–109.
61. Hoiczyk, E., and Hansel, A. (2000). Cyanobacterial cell walls: news from an unusual prokaryotic envelope. J. Bacteriol. *182*, 1191–1199.
62. Komárek, J. (2013). Cyanoprokaryota. 3. Teil/3rd part: heterocytous genera. In Süßwasserflora von Mitteleuropa freshwater flora of Central Europe, B. Büdel, G. Gärtner, L. Krienitz, and M. Schagerl, eds. (Springer Spektrum), p. 1130.
63. Bartley, J.K. (1996). Actualistic taphonomy of cyanobacteria: implications for the Precambrian fossil record. Palaios *11*, 571–586.
64. Strullu-Derrien, C., Fercoq, F., Gèze, M., Kenrick, P., Martos, F., Selosse, M.-A., Benzerara, K., and Knoll, A.H. (2023). Hapalosiphonacean cyanobacteria (Nostocales) thrived amid emerging embryophytes in an early Devonian (407-million-year-old) landscape. iScience *26*, 107338.
65. Coates, J. (2000). Interpretation of Infrared Spectra, a Practical Approach. In Encyclopedia of Analytical Chemistry, R.A. Meyers, ed. (John Wiley & Sons Ltd), pp. 10815–10837.
66. Movasaghi, Z., Rehman, S., and ur Rehman, D.I. (2008). Fourier transform infrared (FTIR) spectroscopy of biological tissues. Appl. Spectrosc. Rev. *43*, 134–179.
67. Marshall, C., Javaux, E., Knoll, A., and Walter, M. (2005). Combined micro-Fourier transform infrared (FTIR) spectroscopy and micro-Raman spectroscopy of Proterozoic acritarchs: a new approach to palaeobiology. Precambrian Res. *138*, 208–224.
68. Sharma, M., Mishra, S., Dutta, S., Banerjee, S., and Shukla, Y. (2009). On the affinity of Chuaria–Tawuia complex: a

multidisciplinary study. Precambrian Res. *173*, 123–136.
69. Loron, C.C., François, C., Rainbird, R.H., Turner, E.C., Borensztajn, S., and Javaux, E.J. (2019). Early fungi from the Proterozoic era in Arctic Canada. Nature *570*, 232–235.
70. Gómez-Ordóñez, E., and Rupérez, P. (2011). FTIR-ATR spectroscopy as a tool for polysaccharide identification in edible brown and red seaweeds. Food Hydrocolloids *25*, 1514–1520.
71. Varnali, T., Edwards, H.G., and Hargreaves, M.D. (2009). Scytonemin: molecular structural studies of a key extremophilic biomarker for astrobiology. Int. J. Astrobiol. *8*, 133–140.
72. Michel, H., Behr, J., Harrenga, A., and Kannt, A. (1998). Cytochrome c oxidase: structure and spectroscopy. Annu. Rev. Biophys. Biomol. Struct. *27*, 329–356.
73. Denisov, I.G., Makris, T.M., Sligar, S.G., and Schlichting, I. (2005). Structure and chemistry of cytochrome P450. Chem. Rev. *105*, 2253–2277.
74. Helliwell, K.E., Lawrence, A.D., Holzer, A., Kudahl, U.J., Sasso, S., Kräutler, B., Scanlan, D.J., Warren, M.J., and Smith, A.G. (2016). Cyanobacteria and eukaryotic algae use different chemical variants of vitamin B12. Curr. Biol. *26*, 999–1008.
75. Didyk, B., Alturki, Y.I.A., Pillinger, C.T., and Eglinton, G. (1975). The petroporphyrins of a Cretaceous oil. Chem. Geol. *15*, 193–208.
76. Zhang, Y., Schulz, F., Rytting, B.M., Walters, C.C., Kaiser, K., Metz, J.N., Harper, M.R., Merchant, S.S., Mennito, A.S., Qian, K., et al. (2019). Elucidating the geometric substitution of petroporphyrins by spectroscopic analysis and atomic force microscopy molecular imaging. Energy Fuels *33*, 6088–6097.
77. Pleyer, H.L., Moeller, R., Fujimori, A., Fox, S., and Strasdeit, H. (2022). Chemical, Thermal, and Radiation Resistance of an Iron Porphyrin: A Model Study of Biosignature Stability. Astrobiology *22*, 776–799.
78. Pierson, B.K., and Castenholz, R.W. (1995). Taxonomy and physiology of filamentous anoxygenic phototrophs. In Anoxygenic photosynthetic bacteria, R.E. Blankenship, M.T. Madigen, and C.E. Bauer, eds. (Kluwer Academic Publisher), pp. 31–47.
79. Swingley, W.D., Blankenship, R.E., and Raymond, J. (2009). In "Evolutionary relationship among purple photosynthetic bacteria and the origin of proteobacterial photosynthetic systems" in The Purple Phototrophic Bacteria, C. Neil Hunter, F. Daldal, M.C. Thurnauer, and J. Thomas Beatty, eds. (Springer), pp. 17–29.
80. Gaisin, V.A., Kalashnikov, A.M., Grouzdev, D.S., Sukhacheva, M.V., Kuznetsov, B.B., and Gorlenko, V.M. (2017). *Chloroflexus islandicus* sp. nov., a thermophilic filamentous anoxygenic phototrophic bacterium from a geyser. Int. J. Syst. Evol. Microbiol. *67*, 1381–1386.
81. Mareš, J., Lara, Y., Dadáková, I., Hauer, T., Uher, B., Wilmotte, A., and Kaštovský, J. (2015). Phylogenetic analysis of cultivation-resistant terrestrial cyanobacteria with massive sheaths (Stigonema spp. and Petalonema alatum, Nostocales, Cyanobacteria) using single-cell and filament sequencing of environmental samples. J. Phycol. *51*, 288–297.
82. Stewart, K.D., and Mattox, K.R. (1975). Comparative cytology, evolution and classification of the green algae with some consideration of the origin of other organisms with chlorophylls a and b. Bot. Rev. *41*, 104–135.
83. Wehr, J.D. (2016). Brown algae (Phaeophyceae) in rivers. In River Algae, O. Necchi, Jr., ed. (Springer), pp. 129–152.
84. Graham, L.D., and Wilcox, L.W. (2000). Algae (Prentice-Hall).
85. Butterfield, N.J., Knoll, A.H., and Swett, K. (1990). A bangiophyte red alga from the Proterozoic of arctic Canada. Science *250*, 104–107.
86. Sutherland, J.E., Lindstrom, S.C., Nelson, W.A., Brodie, J., Lynch, M.D.J., Hwang, M.S., Choi, H.G., Miyata, M., Kikuchi, N., Oliveira, M.C., et al. (2011). A new look at an ancient order: generic revision of the Bangiales (Rhodophyta). J. Phycol. *47*, 1131–1151.
87. Albis-Salas, M.R., and Gavio, B. (2011). Notes on the marine algae of the international biosphere reserve seaflower, Caribbean Colombia IV: new records of macroalgal epiphytes on the seagrass *Thalassia testudinum*. Bot. Mar. *54*, 537–543.
88. Croce, M.E., and Parodi, E.R. (2014). The japanese alga *Polysiphonia morrowii* (Rhodomelaceae, Rhodophyta) on the South Atlantic ocean: first report of an invasive macroalga inhabiting oyster reefs. Helgol. Mar. Res. *68*, 241–252.
89. Titlyanov, E.A., Titlyanova, T.V., Li, X., and Huang, H. (2017). Coral Reef Marine Plants of Coral Reefs (Elsevier).
90. Gonzalez-Esquer, C.R., Smarda, J., Rippka, R., Axen, S.D., Guglielmi, G., Gugger, M., and Kerfeld, C.A. (2016). Cyanobacterial ultrastructure in light of genomic sequence data. Photosynth. Res. *129*, 147–157.
91. Yaylayan, V.A., and Ismail, A.A. (1995). Investigation of the enolization and carbonyl group migration in reducing sugars by FTIR spectroscopy. Carbohydr. Res. *276*, 253–265.
92. Kaplan Can, H., Gurbuz, F., and Odabaşı, M. (2019). Partial characterization of cyanobacterial extracellular polymeric substances for aquatic ecosystems. Aquat. Ecol. *53*, 431–440.
93. Pereira, L., Amado, A.M., Critchley, A.T., Van de Velde, F., and Ribeiro-Claro, P.J. (2009). Identification of selected seaweed polysaccharides (phycocolloids) by vibrational spectroscopy (FTIR-ATR and FT-Raman). Food Hydrocolloids *23*, 1903–1909.
94. Wallace, M.D., Guée, L., Ropartz, D., Fanuel, M., Lannuzel, G., Correc, G., Stubbs, K.A., and Ficko-Blean, E. (2020). Characterisation of an exo-(α-1, 3)-3, 6-anhydro-D-galactosidase produced by the marine bacterium Zobellia galactanivorans DsijT: Insight into enzyme preference for natural carrageenan oligosaccharides and kinetic characterisation on a novel chromogenic substrate. Int. J. Biol. Macromol. *163*, 1471–1479.
95. Usov, A.I. (2011). In "Polysaccharides of the red algae" In Advances in carbohydrate chemistry and biochemistry, D. Horton, ed. (Academic Press), pp. 115–217.
96. Pereira, S., Zille, A., Micheletti, E., Moradas-Ferreira, P., De Philippis, R., and Tamagnini, P. (2009). Complexity of cyanobacterial exopolysaccharides: composition, structures, inducing factors and putative genes involved in their biosynthesis and assembly. FEMS Microbiol. Rev. *33*, 917–941.
97. Honey, D.J. (2012). Heme B in Marine Cyanobacteria and the (Sub-) Tropical North Atlantic (Doctoral dissertation, University of Southampton).
98. Chia, M.A., Kramer, B.J., Jankowiak, J.G., Bittencourt-Oliveira, M.D.C., and Gobler, C.J. (2019). The individual and combined effects of the cyanotoxins, anatoxin-a and microcystin-LR, on the growth, toxin production, and nitrogen fixation of prokaryotic and eukaryotic algae. Toxins *11*, 43.
99. Maraóón, E., Cermeóo, P., Rodríguez, J., Zubkov, M.V., and Harris, R.P. (2007). Scaling of phytoplankton photosynthesis and cell size in the ocean. Limnol. Oceanogr. *52*, 2190–2198.
100. Baludikay, B.K., François, C., Sforna, M.C., Beghin, J., Cornet, Y., Storme, J.Y., Fagel, N., Fontaine, F., Littke, R., Baudet, D., et al. (2018). Raman microspectroscopy, bitumen reflectance and illite crystallinity scale: comparison of different geothermometry methods on fossiliferous Proterozoic sedimentary basins (DR Congo, Mauritania and Australia). Int. J. Coal Geol. *191*, 80–94.
101. Lewan, M.D., and Maynard, J.B. (1982). Factors controlling enrichment of vanadium and nickel in the bitumen of organic sedimentary rocks. Geochem. Cosmochim. Acta *46*, 2547–2560.
102. Saito, M.A., Sigman, D.M., and Morel, F.M. (2003). The bioinorganic chemistry of the ancient ocean: the co-evolution of cyanobacterial metal requirements and biogeochemical cycles at the Archean–Proterozoic boundary? Inorg. Chim. Acta. *356*, 308–318.
103. Russell, M.J. (2022). Cobalt: A must-have element for life and livelihood. Proc. Natl. Acad. Sci. USA *119*, e2121307119.
104. Saito, M.A., Moffett, J.W., Chisholm, S.W., and Waterbury, J.B. (2002). Cobalt limitation and uptake in Prochlorococcus. Limnol. Oceanogr. *47*, 1629–1636.
105. Sunda, W.G., and Huntsman, S.A. (1995). Cobalt and zinc interreplacement in marine phytoplankton: Biological and geochemical implications. Limnol. Oceanogr. *40*, 1404–1417.
106. Roth, J.R., Lawrence, J.G., and Bobik, T.A. (1996). Cobalamin (coenzyme B12): synthesis and biological significance. Annu. Rev. Microbiol. *50*, 137–181.
107. Huertas, M.J., López-Maury, L., Giner-Lamia, J., Sánchez-Riego, A.M., and Florencio, F.J. (2014). Metals in cyanobacteria: analysis of the copper, nickel, cobalt and arsenic homeostasis mechanisms. Life *4*, 865–886.
108. Cavet, J.S., Borrelly, G.P.M., and Robinson, N.J. (2003). Zn, Cu and Co in cyanobacteria: selective control of metal availability. FEMS Microbiol. Rev. *27*, 165–181.
109. Sforna, M.C., Daye, M., Philippot, P., Somogyi, A., van Zuilen, M.A., Medjoubi, K., Gérard, E., Jamme, F., Dupraz, C., Braissant, O., et al. (2017). Patterns of metal distribution in hypersaline microbialites during early diagenesis: implications for the fossil record. Geobiology *15*, 259–279.
110. Pedersén, M., Saenger, P., Rowan, K.S., and Hofsten, A.V. (1979). Bromine, bromophenols and floridorubin in the red alga Lenormandia prolifera. Physiol. Plantarum *46*, 121–126.
111. Gribble, G.W. (1999). The diversity of naturally occurring organobromine compounds. Chem. Soc. Rev. *28*, 335–346.

112. Caspi, R., Billington, R., Keseler, I.M., Kothari, A., Krummenacker, M., Midford, P.E., Ong, W.K., Paley, S., Subhraveti, P., and Karp, P.D. (2020). The MetaCyc database of metabolic pathways and enzymes-a 2019 update. Nucleic Acids Res. *48*, D445–D453.
113. Croft, W.N., and George, E.A. (1959). Blue-green algae from the Middle Devonian of Rhynie. Aberdeenshire. Bull. Brit. Mus. Nat. Hist. Geol. *3*, 341–353.
114. Komárek, J., Kaštovský, J., Mareš, J., and Johansen, J.R. (2014). Taxonomic classification of cyanoprokaryotes (cyanobacterial genera) 2014, using a polyphasic approach. Preslia *86*, 295–335.
115. Allen, J.F., Thake, B., and Martin, W.F. (2019). Nitrogenase inhibition limited oxygenation of Earth's Proterozoic atmosphere. Trends Plant Sci. *24*, 1022–1031.
116. Dos Santos, P.C., Fang, Z., Mason, S.W., Setubal, J.C., and Dixon, R. (2012). Distribution of nitrogen fixation and nitrogenase-like sequences amongst microbial genomes. BMC Genom. *13*, 1–12.
117. Stüeken, E.E., Buick, R., Guy, B.M., and Koehler, M.C. (2015). Isotopic evidence for biological nitrogen fixation by molybdenum-nitrogenase from 3.2 Gyr. Nature *520*, 666–669.
118. Schirrmeister, B.E., de Vos, J.M., Antonelli, A., and Bagheri, H.C. (2013). Evolution of multicellularity coincided with increased diversification of cyanobacteria and the Great Oxidation Event. Proc. Natl. Acad. Sci. USA *110*, 1791–1796.
119. Uyeda, J.C., Harmon, L.J., and Blank, C.E. (2016). A comprehensive study of cyanobacterial morphological and ecological evolutionary dynamics through deep geologic time. PLoS One *11*, e0162539.
120. Sánchez-Baracaldo, P., Raven, J.A., Pisani, D., and Knoll, A.H. (2017). Early photosynthetic eukaryotes inhabited low-salinity habitats. Proc. Natl. Acad. Sci. USA *114*, E7737–E7745.
121. Schirrmeister, B.E., Gugger, M., and Donoghue, P.C.J. (2015). Cyanobacteria and the Great Oxidation Event: evidence from genes and fossils. Palaeontology (Prague) *58*, 769–785.
122. Solé, V., Papillon, E., Cotte, M., Walter, P., and Susini, J. (2007). A multiplatform code for the analysis of energy-dispersive X-ray fluorescence spectra. Spectrochim. Acta B Atom Spectrosc. *62*, 63–68.
123. Ravel, B., and Newville, M. (2005). ATHENA, ARTEMIS, HEPHAESTUS: data analysis for X-ray absorption spectroscopy using IFEFFIT. J. Synchrotron Radiat. *12*, 537–541.
124. Cahen, L., Snelling, N.J., Delhal, J., Vail, J.R., Bonhomme, M., and Ledent, D. (1984). The Geochronology and Evolution of Africa (Clarendon)), p. 512.
125. Delvaux, D., Maddaloni, F., Tesauro, M., and Braitenberg, C. (2021). The Congo Basin: stratigraphy and subsurface structure defined by regional seismic reflection, refraction and well data. Global Planet. Change *198*, 103407.
126. Grey, K. (1999). A Modified Palynological Preparation Technique for the Extraction of Large Neoproterozoic Acanthomorph Acritarchs and Other Acid-Insoluble Microfossils (Western Australia Geological Survey). Record 1999/10.
127. Lin, R., and Patrick Ritz, G. (1993). Studying individual macerals using i.r. microspectroscopy, and implications on oil versus gas/condensate proneness and "low-rank" generation. Org. Geochem. *20*, 695–706.
128. Sekkal, M., Huvenne, J.P., Legrand, P., Sombret, B., Mollet, J.C., Mouradi-Givernaud, A., and Verdus, M.C. (1993). Direct structural identification of polysaccharides from red algae by FTIR microspectroscopy I: Localization of agar in *Gracilaria verrucosa*, sections. Mikrochim. Acta *112*, 1–10.
129. Alstadt, K.N., Katti, D.R., and Katti, K.S. (2012). An *in situ* FTIR step-scan photoacoustic inverstigation of kerogen and minerals in oil shale. *Spectrochim*. Acta A Mol. Biomol. Spectrosc., Spectrochim Acta A *89*, 105–113.

STAR★METHODS

KEY RESOURCES TABLE

REAGENT or RESOURCE	SOURCE	IDENTIFIER
Bacterial and virus strains		
Stigonema robustum	Mareš et al., 2015[81] (CBFS herbarium of the botany department of the University of South Bohemia (České Budějovice, Czech Republic)	CBFS-A027
Stigonema informe	Mareš et al., 2015[81] (CBFS herbarium of the botany department of the University of South Bohemia (České Budějovice, Czech Republic)	CBFS-A033
Stigonema turfaceum	Mareš et al., 2015[81] (CBFS herbarium of the botany department of the University of South Bohemia (České Budějovice, Czech Republic)	CBFS-A031
Stigonema ocellatum	Göttingen university "The *Sammlung von Algenkulturen der Universität Göttingen" (SAG)*	SAG 48.90
Calothrix sp.	Belgian Culture Collection of Microorganisms/ Université of Liège Cyanobacteria collection	BCCM/ULC003
Bangiopsis franklynottii	Bigelow Laboratory for Ocean Sciences National Center for Marine Algae and Microbiota collection	CCMP3416
Critical commercial assays		
LR White embedding kit	Sigma-Aldrich	62662-1EA-F
Araldite/Embed EMBEDDING kit (Mollenhauer formula)	Electron Microscopy Sciences	Cat. #13940
Experimental models: Organisms/strains		
Microfossils *Polysphaeroides filiformis*	This paper (Early Life Traces and Evolution – Astrobiology Laboratory (UR Astrobiology))	N/A
Software and algorithms		
AxioVision SE64 Rel. 4.9.1.	Zeiss	https://www.micro-shop.zeiss.com/en/us/system/axiovision+software/software+axiovision/axiovision+program/410130-0909-000
Rstudio 4.1.1	RStudio Team, 2020	https://posit.co/download/rstudio-desktop/
Wire 4.2	Renishaw	Renishaw: enhancing efficiency in manufacturing and healthcare
OPUS 8.0	Bruker	Bruker Optik GmbH 2017
PyMCA	Solé et al., 2007[122]	http://www.silx.org/doc/PyMca/dev/index.html
Athena	Ravel and Newville, 2005[123]	https://bruceravel.github.io/demeter/
Inkscape	Inkscape Project, 2020	https://inkscape.org/fr/
MatLab	MathWorks	https://www.mathworks.com/products/matlab.html
Other		
XRF Reference Sample	AXO Dresden GmbH	RF7-200-S2372

RESOURCE AVAILABILITY

Lead contact

Emmanuelle J. Javaux (ej.javaux@uliege.be)

Materials availability

Fossil material is part of the collections of the Early Life Traces & Evolution-Astrobiology (UR Astrobiology-ULiege). Material and data are available upon reasonable request to lead contact.

Data and code availability

- All data reported in this paper are available upon request to the lead contact.
- This paper does not report original code.
- Any additional information required to reanalyze the data reported in this work paper is available from the lead contact upon request.

EXPERIMENTAL MODEL AND STUDY PARTICIPANT DETAILS

Fresh modern cyanobacteria and red alga

In order to compare morphometric traits of microfossils with modern cyanobacterial analogues, three herbaria of the genus *Stigonema* (CBFS-A033: *S. informe*, CBFS-A027: *S. robustum*, CBFS-A031 *S. turfaceum*) described by Mareš et al. (2015)[81] were obtained from the CBFS herbarium of the botany department of the University of South Bohemia (České Budějovice, Czech Republic). *Stigonema ocellatum* SAG 48.90 was obtained from the culture collection of algae at Göttingen university "The *Sammlung von Algenkulturen der Universität Göttingen" (SAG)* and empty scytonemin-pigmented sheaths of a dead culture of the strain *Calothrix* sp. BCCM/ULC003 obtained from the Belgian Culture Collection of Microorganisms/Université of Liège Cyanobacteria collection. The red alga *B. franklynottii* CCMP3416 (formerly *B. subsimplex*) was compared as eukaryotic potential analogue based on morphological similarities. The strain CCMP3416 was obtained from the Bigelow Laboratory for Ocean Sciences National Center for Marine Algae and Microbiota collection. *B. franklynottii* CCMP3416 was grown under constant lightning at 20°C in liquid L1Si medium purchased at the culture collection.

Geological context and microfossils preparation

Microfossils in this study come from the Kanshi SB13 core, drilled through the BII group of the Mbuji-Mayi Supergroup (see Figure S18). Drilling was performed in the 1950's in Democratic Republic of Congo and the drill core is stored in the collections of the Geodynamic and Mineral Resource Service, at the Royal Museum for Central Africa, Tervuren, Belgium. The Congo Basin is an intracratonic basin localized in Central Africa and covers four countries (Angola, Democratic Republic of Congo, Central African Republic, and Republic of the Congo) with an area of 1,200,000 km^2.[100] The BII Group of the Mbuji-Mayi Supergroup has been dated at 948 $\pm$20 Ma based on the K-Ar dating of dolerites covering and intruding the Mbuyi-Mayi Supergroup.[124] Biostratigraphy using acritarchs indicates a late Mesoproterozoic to early Neoproterozoic age.[42] A recently revised study of the stratigraphy and tectonic evolution of the Congo Basin using geological and seismic data places the whole Mbuyi-Mayi Supergroup as older than 1 Ga.[125] Recently, the upper BII Group has been dated more precisely between 1030 – 1040 Ma to 1006 Ma using the Re-Os method on kerogen of shales and Ar-Ar, Sm-Nd and U-Pb methods on dolerites.[43]

Microfossils were extracted using a protocol modified from Grey (1999).[126] This modified protocol avoids centrifugation, which could damage the organic-walled microfossils. It consisted of acid demineralization, with HCl 35% to remove carbonates, followed by HF 60% to remove silicates, and a final acid treatment with hot HCl 35% to remove neo-formed fluorides. Neutralization with Milli-Q water were performed between each acid maceration. The organic residues were filtered and stored in Milli-Q water. A fraction of these macerates was mounted on microscopic slides for optical microscopy. Fossil specimens were pipetted under an inverted microscope to prepare samples for SEM, TEM, Raman and FT-IR microspectroscopies and SR-nanoXRF and SR-μXANES techniques.

METHOD DETAILS

Light microscopy

Macerates containing *P. filiformis* were mounted on microscopic slides, as well as filaments of both modern *Stigonema* and *B. franklynottii* specimens. These slides were observed with a Zeiss Axio imager microscope equipped with an Axiocam MRc5 camera. The images of microfossils (n=30) of interest, *S. robustum* (n=12), *S. turfaceum* (n=19), *S. informe* (n=12) and *B. franklynottii* (n=22) and measurements of their different features were made with the AxioVision SE64 Rel. 4.9.1 software. Boxplot graph using these measurements was made using Rstudio 4.1.1 software.

Raman microspectroscopy

One isolated microfossil was pipetted under a Nikon Eclipse Ts2 inverted microscope, placed onto ZnSe plates and air-dried. It was analyzed by Raman microspectroscopy to confirm the thermal maturity of the kerogenous wall (see[98]). These analyses were made in the Early Life Traces & Evolution – Astrobiology laboratory (ULiège) on a Renishaw Invia Raman microspectrometer with an Air-ion-40 mW monochromatic 514 nm laser

source. In order to obtain a spot size of 1 – 2 μm, the laser was focused using an objective x 100. Spectra were obtained on 10 points for each structure of *P. filiformis:* the sheath, cell walls and internal dark inclusions (ICIs) on one extracted specimen. These spectra were acquired with a laser power of 0.1%, to avoid irreversible damage on samples, and with an integration time of 10x1 sec. They were also obtained with a static mode enabling spectra ranging from 1 cm^{-1} to 2000 cm^{-1} and centered at 1150 cm^{-1}. Acquisitions were obtained using a 1800 l/mm grating that illuminates a CCD array detector of 1040 x 256 pixels. Spectra were finally processed with Wire 4.2® software of Renishaw and with RStudio 4.1.1 software. Paleothermometry was estimated based on the Raman reflectance method (see Figure S2; Table S3 and ref.[100]).

FT-IR microspectroscopy

In order to investigate the molecular composition of *P. filiformis* kerogens and compare it to possible analogs, Fourier-transform infrared microspectroscopy (FT-IR) was performed on 10 microfossils, and on modern specimens including filaments of *B. franklynottii* CCMP3416, filaments of *S. ocellatum* SAG 48.90 obtain from the culture collection of algae at Göttingen university *"The Sammlung von Algenkulturen der Universität Göttingin" (SAG)* and empty scytonemin-pigmented sheaths of a dead culture of the strain *Calothrix* sp. BCCM/ULC003 obtained from the Belgian Culture Collection of Microorganisms /Université of Liège Cyanobacteria collection. Fourier-transform infrared spectroscopy (FT-IR) is a fast, non-destructive method permitting to analyze the molecular structure and bonding information of molecules contained in a sample. Isolated microfossils were pipetted under a Nikon Eclipse Ts2 inverted microscope, deposited onto ZnSe plates and air-dried. After three successive washings in miliQ water, sheaths of dead culture of *Calothrix* sp. BCCM/ULC003 were spotted onto a ZnSe plate, single filaments of *B. franklynottii* (n= 6) were spotted onto a ZnSe plate. Plates were air-dried before analysis. Modern and fossil samples were analyzed with a Hyperion 2000 Bruker microscope coupled to a Tensor 27 FT-IR spectrometer (Early Life Traces and Evolution–Astrobiology Laboratory, University of Liège, Belgium). Spectra were collected with a conventional Globar source equipped with 15× objective (NA = 0.4) and a liquid-nitrogen-cooled MCT-A detector. Background was obtained by accumulating 1024 scans on a spot free of microfossils of the ZnSe plate. Spectra were obtained with a resolution of 4 cm^{-1} in transmission mode by combining 512 or 1024 scans for each microfossil and modern specimens. The spectra were then processed (automatic atmospheric compensation and baseline subtraction) with the OPUS 8.0 software. Band values were determined on spectra and based on the second derivatives. Then, their assignments were made using several references about FT-IR analyzes on microfossils and modern organisms (Table S16).[47,65–67,70,71,92,127–129] For *S. ocellatum* SAG 48.90, strain was cultured in BG110 agar medium[25] at a temperature of 20°C and with a constant white LED illumination (5-20 μmol photon m^{-2} s^{-1}).

Synchrotron-based nano X-ray fluorescence (SR-nanoXRF)

Microfossils were pipetted under a Nikon Eclipse Ts2 inverted microscope and were deposited on silicon nitride (Si_3N_4) windows, before being air-dried. SR-nanoXRF was performed on 8 specimens of *P. filiformis* ICIs within fossil cells. Fossil samples were analyzed at the Synchrotron Soleil (Nanoscopium beamline, Gif-sur-Yvette, France), and at the European Synchrotron Radiation Facility (ID16B beamline, ESRF, Grenoble, France). The distribution of metals in fossils and modern filaments was characterized with energy of excitation of 12 keV at Synchrotron Soleil and the maps were acquired with pixels between 150 and 300 nm^2. This energy of excitation allowed the detection of elements between Si and As (K lines). At ESRF, maps were acquired with energy of excitation of 17.5 keV and with pixels between 100 and 300 nm^2. This energy of excitation allowed the detection of elements between Si and Y (K lines). Fossils were also investigated at the on the microXAS-X05LA beamline (Swiss Light Source, microXAS beamline, Villigen, Switzerland) with energy of excitation of 8.4 keV, allowing detection between Si and Ni (K Lines) in order to identify the zones of interest for SR-μXANES investigation. Soleil synchrotron and ESRF are called nano-XRF due to the size of the beam (few tens of nm) and to the size of pixels in maps. In SLS, the beam is ∼1μm and is thus called as μXRF or μXANES.

Synchrotron-based micro X-ray absorption spectroscopy (SR-μXANES)

XANES was performed in fluorescence mode with a beam spot-size focused to ∼1 μm and an incident X-ray energy selected with a Si (1 1 1) double crystal monochromator at SLS (Swiss Light Source, microXAS beamline, Villigen, Switzerland) on the microXAS-X05LA beamline. XANES analyses were made on Ni-rich spots highlighted by the SR-μXRF mapping on 3 *P. filiformis* specimens. For each point, 3 to 4 replicate spectra were acquired in fluorescence mode by measuring the Ni K-edge (8.33 keV) and tuning the monochromator energy from 8.24 to 8.71 keV. The K-edge of a Nickel (0) foil (8.333 keV) was used to perform the energy calibration. Reference compounds ($(Ni(OH)_2$, NiO, $NiCO_3$, Ni_3S_2, $NiSO_4(H_2O)_{6-7}$) were also recorded in transmission mode. XANES spectra for Ni octaethyl porphyrin (NiOEP), Ni tetraphenyl porphyrin (NiTPP) and asphaltene were retrieved from literature (52, 125). Data were normalized using the Athena® software.[123] Linear combination fitting (LCF; see Table S12) was performed in the range between -30 eV to +100 eV relative to the theoretical Ni K-edge energy (8333 eV), following Nesbitt et al.(2017).[57] The assessment of the quality of the fitting was done by looking the smallest R-factor and the combination of components. Concentration of Ni in ICIs was estimated using a thin film XRF Reference Sample (RF7-200-S2372, AXO Dresden GmbH) and by using the method of Sforna et al. (2022).[46] The equations and their results are summarized in the Table S9.

Scanning electron microscopy (SEM)

Four isolated microfossils were pipetted under a Nikon Eclipse Ts2 inverted microscope and deposited on glass slides and left to air-dry in closed petri dish. Slides were coated with carbon of 200 Å and then were observed using a JEOL JSM-7800F LV (JEOL) in secondary electron mode, with a voltage of 5 kV at the Centre Commun de Microscopie de Lille (Unité Matériaux et Transformations, University of Lille, France).

Transmission Electron Microscopy (TEM)

For the ultrastructural characterization, filaments of *B. franklynottii* were fixed using 2,5 %-glutaraldehyde solution in 0.1 M cacodylate buffer at pH 7.4. This fixation consists to three baths of PBS solution. After each bath and after a centrifugation at 11,000 *g*, the supernatant was removed. Following PBS baths, filaments were placed in a bath of the glutaraldehyde solution for one hour. Finally, the glutaraldehyde solution was removed and filaments were stored in 0.2 M cacodylate buffer at 4°C.

Four isolated microfossils and several culture filaments of *S. robustum* CBFS-A027 and *B. franklynottii* CCMP3416 were embedded in agarose (1%) and dehydrated in a graded ethanol series (15%, 30%, 50%, 70%, 90% and 100% ethanol). Thereafter, microfossils were progressively included within pure London Resin White and finally heated for polymerization for 1 hour at 40°C and at 60°C for 24 hours, while filaments of modern analogues were progressively included within epon resin and finally heated for polymerization at 60°C for at least 2 days. The resulted blocks were cut into transversal ultrathin sections with a diamond knife on an ultramicrotome Reichert Ultracut E. The ultrathin sections were then deposited on formvar-coated copper grids (400 mesh) for observations. Samples (microfossils) were observed in a STEM Tecnai G^2 Twin (CAREM platform, University of Liège, Belgium), samples (*Bangiopsis* and *Stigonema*) were observed with a TEM Tecnai Spirit T12 (Microscopy CORE Lab, University of Maastricht, The Netherlands), and (only fossils) with a STEM FEI TITAN THEMIS 300 (Centre Commun de Microscopie de Lille, Unité Matériaux et Transformations, University of Lille, France), at accelerating voltages of 200 kV, 120kV and 300 kV respectively.

QUANTIFICATION AND STATISTICAL ANALYSIS

The statistical treatment of morphometric data was performed using Rstudio 4.1.1 and Excel software. Concentration of Ni in ICIs was estimated using the method of Sforna et al. (2022).[46] The equations and their results are summarized in the Table S9. Paleothermometry was calculated using the mean of Raman Reflectance data (Figure S2; Table S3 and ref.[100]).